



HAL
open science

Non-Parametric GraphNet-Regularized Representation of dMRI in Space and Time

Rutger H.J. Fick, Alexandra Petiet, Mathieu Santin, Anne-Charlotte
Philippe, Stéphane Lehericy, Rachid Deriche, Demian Wassermann

► **To cite this version:**

Rutger H.J. Fick, Alexandra Petiet, Mathieu Santin, Anne-Charlotte Philippe, Stéphane Lehericy, et al.. Non-Parametric GraphNet-Regularized Representation of dMRI in Space and Time. *Medical Image Analysis*, 2018, 43, pp.37–53. 10.1016/j.media.2017.09.002 . hal-01578296

HAL Id: hal-01578296

<https://inria.hal.science/hal-01578296>

Submitted on 28 Aug 2017

HAL is a multi-disciplinary open access archive for the deposit and dissemination of scientific research documents, whether they are published or not. The documents may come from teaching and research institutions in France or abroad, or from public or private research centers.

L'archive ouverte pluridisciplinaire **HAL**, est destinée au dépôt et à la diffusion de documents scientifiques de niveau recherche, publiés ou non, émanant des établissements d'enseignement et de recherche français ou étrangers, des laboratoires publics ou privés.

Non-Parametric GraphNet-Regularized Representation of dMRI in Space and Time

Rutger H.J. Fick^a, Alexandra Petiet^b, Mathieu Santin^b, Anne-Charlotte Philippe^b, Stephane Lehericy^b, Rachid Deriche^a, Demian Wassermann^{a,*}

^a *Université Côte d'Azur, Inria, France*

^b *CENIR, Institut du Cerveau et de la Moelle épinière, Paris, France*

Abstract

Effective representation of the four-dimensional diffusion MRI signal – varying over three-dimensional q-space and diffusion time τ – is a sought-after and still unsolved challenge in diffusion MRI (dMRI). We propose a functional basis approach that is specifically designed to represent the dMRI signal in this $q\tau$ -space. Following recent terminology, we refer to our $q\tau$ -functional basis as “ $q\tau$ -dMRI”. $q\tau$ -dMRI can be seen as a time-dependent realization of q-space imaging by Paul Callaghan and colleagues. We use GraphNet regularization – imposing both signal smoothness and sparsity – to drastically reduce the number of diffusion-weighted images (DWIs) that is needed to represent the dMRI signal in the $q\tau$ -space. As the main contribution, $q\tau$ -dMRI provides the framework to – without making biophysical assumptions – represent the $q\tau$ -space signal and estimate *time-dependent* q-space indices ($q\tau$ -indices), providing a new means for studying diffusion in nervous tissue. We validate our method on both *in-silico* generated data using Monte-Carlo simulations and an *in-vivo* test-retest study of two C57Bl6 wild-type mice, where we found good reproducibility of estimated $q\tau$ -index values and trends. In the hopes of opening up new τ -dependent venues of studying nervous tissues, $q\tau$ -dMRI is the first of its kind in being specifically designed to provide open interpretation of the $q\tau$ -diffusion signal.

1. Introduction

Probing brain tissue structure with time-dependent properties of the diffusion MRI (dMRI) signal is gaining momentum in the dMRI community (see e.g. Moonen et al., 1991; Le Bihan, 1995; Assaf et al., 1998; Novikov et al., 2014; De Santis et al., 2016; Ning et al., 2016; Fieremans et al., 2016). Yet, effectively representing the four-dimensional dMRI signal – varying over three-dimensional q-space and diffusion time – is still a sought-after and unsolved challenge. To specifically represent the dMRI signal in this $q\tau$ -space, which has been coined by Novikov et al. (2016), we propose a $q\tau$ -functional basis approach that we appropriately refer to as “ $q\tau$ -dMRI”. As the main contribution, $q\tau$ -dMRI provides the framework to – without making biophysical assumptions – represent the $q\tau$ -space signal and estimate *time-dependent* q-space indices ($q\tau$ -indices), providing a new means for studying diffusion in nervous tissue.

*Corresponding author

Email address: demian.wassermann@inria.fr (Demian Wassermann)

Diffusion time dependence (τ -dependence) in brain MRI was initially studied to find proof of diffusion restriction in tissue (Moonen et al., 1991; Le Bihan, 1995; Assaf et al., 1998). In these studies, the existence of restricting tissue boundaries would be proved by a change in apparent diffusion coefficient over time¹. While the concept of diffusion restriction inside nervous tissue is now established (Beaulieu, 2002), the interpretation and significance of τ -dependence is still under debate. Earlier works use τ -dependent models of perpendicular, intra-axonal diffusion to separate intra- from extra-axonal signal contributions (Assaf et al., 2004, 2008). Though, these studies note that the intra-axonal diffusion signal is probably already restricted for the shortest possible diffusion times for Pulsed-Gradient Spin-Echo (PGSE) protocols (10-20ms) inside realistically sized axons ($< 2\mu\text{m}$) (Aboitiz et al., 1992). If this is true, models for intra-axonal τ -dependence cannot account for the observed τ -dependence at longer diffusion times (Fieremans et al., 2016). Recent studies argue that perpendicular τ -dependence originates from the extra-axonal space, where diffusion is restricted due to axon packing (Novikov et al., 2014; Burcaw et al., 2015). So far, these features have been studied both at clinical gradient strengths using τ -dependent diffusion coefficients (Fieremans et al., 2016) and at high gradient strengths using perpendicular, “AxCaliber”-style acquisition schemes (De Santis et al., 2016). Studies exploring τ -dependence at high gradient strengths and multiple directions in general tissue geometries are very demanding in terms of diffusion measurements and acquisition time. To reduce the required number of measurements, we propose an approach centered on regularized functional bases for the representation of the $q\tau$ -dMRI signal.

To characterize the diffusion signal at higher gradient strengths for a *fixed* diffusion time, q -space techniques can reconstruct the Ensemble Average Propagator (EAP) by assuming the narrow pulse approximation ($\delta \rightarrow 0$). In doing so, these methods are able to conveniently interpret the signal as the EAP through a Fourier transform (Tanner and Stejskal, 1968; Callaghan, 1991). The EAP describes the probability density $P(\mathbf{R}; \tau)$ that a particle experiences a displacement \mathbf{R} for a given τ . As τ increases, the likelihood that particles travel further increases in unrestricted neuronal tissues (Cohen and Assaf, 2002). In 1D-NMR, q -space indices such as the Return-to-Origin Probability (RTOP) (Hürlimann et al., 1995) have a microstructural interpretation quantifying the dynamic connectivity of pore spaces (Mitra et al., 1995). Furthermore, the τ -dependence of RTOP and the Mean Squared Displacement (MSD) has been marked as a possible feature for microscopic tissue alterations (Özarslan et al., 2006, 2012).

The estimation of q -space indices has been generalized from 1D-NMR to spherical and three-dimensional q -space acquisitions to improve their applicability as non-invasive descriptors of nervous tissue. This development inspired modeling approaches such as q -ball imaging (Tuch, 2004), 3D Cartesian sampling-based diffusion spectrum MRI (Wedeen et al., 2005), and multi-shell hybrid diffusion imaging (Wu et al., 2008). However, numerical implementations of these techniques to reconstruct the EAP require dense acquisition schemes, making them impractical when scanning time is limited. The introduction of functional bases to efficiently represent the dMRI signal partly overcame this restriction (see e.g. Descoteaux et al., 2007; Assemlal et al., 2009; Özarslan et al., 2013b). That is, the fitting of these representations can be regularized using properties such as smoothness, sparsity, and positivity of the EAP. This allows for more accurate EAP and tissue property recovery using fewer samples, resulting in faster acquisition schemes. Despite these advances, the influence of τ -dependence in EAP recovery and q -space index estimation is overlooked. To include τ -dependence, we propose a method that generalizes EAP reconstruction over varying

¹Interestingly, the first study actually found no evidence of diffusion restriction.

diffusion times.

We propose a functional basis approach that represents the 4D $q\tau$ -space signal using the cross-product of two separable functional bases – one over 3D q -space and another over 1D diffusion time. This formulation allows us to stand on the shoulders of giants; allowing us to freely incorporate any previously proposed functional basis approach and regularization technique within our own framework. As our q -space basis, we choose the Mean Apparent Propagator (MAP) *Fourier* basis for its efficient signal representation (Ning et al., 2015) and wide range of closed-form q -space indices (Özarslan et al., 2013b; Fick et al., 2016c). Our temporal basis is novel and is designed to effectively represent both free and restricted diffusion over τ . Following the terminology of Novikov et al. (2016) and colleagues, we refer to our formulation of this $q\tau$ -basis as “ $q\tau$ -dMRI”.

When representing the $q\tau$ -space, it is important to be robust to acquisition noise and do so efficiently using few measurements. As a solution, we regularize the fitting of $q\tau$ -dMRI by imposing both signal smoothness and signal sparsity. Our arguments for including each of these regularization strategies in our framework are the following: First, imposing signal smoothness using the Laplacian of the reconstructed signal has shown to be effective in dMRI reconstruction (Descoteaux et al., 2007; Caruyer and Deriche, 2012; Fick et al., 2016c). Its benefits within our framework are threefold: it reduces oscillations, it provides smooth inter- and extrapolation between measured $\{q, \tau\}$ points; it promotes positive EAP reconstruction, though not explicitly; and estimation of the Laplacian of the reconstructed signal in $q\tau$ -dMRI is *analytic*. Secondly, imposing signal sparsity in the parameter space of a functional basis has been previously introduced as *continuous* compressed sensing (CS) in dMRI reconstruction (e.g. Michailovich and Rathi, 2008; Merlet and Deriche, 2013; Rathi et al., 2014; Paquette et al., 2015). A continuous CS framework is advantageous because it is not acquisition dependent and enables data inter- and extrapolation. In particular, Merlet and Deriche (2013) point out the efficiency of using the isotropic equivalent of our spatial MAP basis in continuous CS, which enabled them to accurately reconstruct the 3D-EAP with as little as 32 samples. Our double regularization strategy can be seen as modified Elastic-Net regularization (Zou and Hastie, 2005) along the same lines as GraphNet (Grosenick et al., 2013), where the standard ℓ_2 -norm penalty term has been replaced with the norm of the Laplacian of the reconstructed signal. As they show in their work, this modification explicitly imposes structure on the estimated model parameters, while also enforcing a sparse representation.

Once the basis coefficients are estimated, $q\tau$ -dMRI effectively represents both the $q\tau$ -space signal attenuation and EAP at finite q and τ . This allows for the time-dependent estimation of any previously proposed q -space indices which we call $q\tau$ -indices for brevity. Contrary to previous studies that could only explore $q\tau$ -indices in one predetermined direction (Özarslan et al., 2006, 2012), $q\tau$ -dMRI allows for the estimation of $q\tau$ -indices along any direction, greatly enhancing their practical applicability. Furthermore, $q\tau$ -dMRI can also be used as a signal preprocessing step for subsequent parametric modeling of the $q\tau$ -space, as done by Fick et al. (2016c) with q -space indices.

We validate our method on both *in-silico* generated data using Monte-Carlo simulations in Camino (Cook et al., 2006) and an *in-vivo* test-retest study of two C57Bl6 wild-type mice. On the Camino data, we illustrate the robustness of $q\tau$ -dMRI in representing the $q\tau$ -signal attenuation in the presence of noise and severely subsampled data. On the *in-vivo* data, we demonstrate the reproducibility of $q\tau$ -indices in the corpus callosum, where we show that time-dependence of $q\tau$ -indices corresponds with expected biological properties. We present the graphical abstract of our work in Figure 1.

[Figure 1 about here.]

2. Theory

In this section, we first provide the biological relevance of studying diffusion time in biological tissues in Section 2.1. We then explain the relation between the measured $q\tau$ -diffusion signal and the four-dimensional EAP in Section 2.2. We then describe the properties and implementation of our $q\tau$ -dMRI methodology in Section 2.3.

2.1. Biological Relevance of Diffusion Time

In a fluid, water particles follow random paths according to Brownian motion (Einstein, 1956). When we consider an *ensemble* of these particles in a volume, we can describe their average probability density $P(\mathbf{R}, \tau)$ that a particle will experience a displacement $\mathbf{R} \in \mathbb{R}^3$ during diffusion time $\tau \in \mathbb{R}^+$. This quantity is often referred to as the ensemble average propagator (EAP) (Kärger and Heink, 1983). In a free solution, the EAP can be described by a Gaussian distribution as

$$P(\mathbf{R}; \tau) = \frac{1}{(4\pi D\tau)^{3/2}} e^{-\frac{\|\mathbf{R}\|^2}{4D\tau}} \quad (1)$$

where D is the diffusion coefficient. Eq. (1) shows that the likelihood that particles travel further increases when either D or τ increases. While keeping D constant, this concept can be made clear using isocontours such that $P(\mathbf{R}, \tau) = c$ with $c > 0$. Figure 2 shows the same isocontour for diffusion times $\tau_1 < \tau_2 < \tau_3$ in four schematic representations of different tissue types. As can be seen by the growth of the isocontours, using longer τ increases the likelihood that particles travel further. The shape of the isocontour depends on the structure of the surrounding tissue. From left to right, in free water, where Eq. (1) is a good approximation, particles are unrestricted and travel furthest with isotropic, Gaussian probability. Next, at a coarse diffusion scale, gray matter tissue can often be seen as generally unorganized and hinders diffusion equally in all directions (Jones, 2010). For this reason, these tissues also produce isotropic contours, but smaller than those in free water. In axon bundles, here illustrated as gray lines, axons are mostly aligned with the bundle axis. Particle movement is restricted perpendicular to this direction and is relatively free along it, causing *anisotropic* isocontours (Beaulieu, 2002). Finally, in areas where two bundles cross there is a mix between the isocontours of each bundle.

[Figure 2 about here.]

Note that we intentionally drew the isocontours for τ_1 more isotropic than those of τ_3 in the right two white matter tissues. For shorter τ , particles have not had much time to interact with surrounding tissue, resulting in a similar probability that a particle travels in any direction. The isocontours for very short τ will therefore always be isotropic. For longer τ , particles have had more time to interact with the tissue, either traveling far along a relatively unrestricted direction or staying close to its origin along a restricted direction, resulting in more anisotropic profiles (Tanner, 1978). Describing this tissue with a 3D diffusion tensor \mathbf{D} , this means that the perpendicular diffusivity D_{\perp} becomes τ -dependent and decreases as τ increases (Cohen and Assaf, 2002). Different tissue types will induce different τ -dependence of the EAP (Özarslan et al., 2006, 2012). In the next sections, we will show how we can use $q\tau$ -dMRI to estimate $P(\mathbf{R}; \tau)$ and explore the τ -dependence of the four-dimensional EAP.

2.2. The Four-Dimensional Ensemble Average Propagator

In dMRI, the EAP is estimated from a set of diffusion-weighted images (DWIs). A DWI is obtained by applying two sensitizing diffusion gradients of pulse length δ to the tissue, separated by separation time Δ . The resulting signal is ‘weighted’ by the average particle movements along the applied gradient direction. Using the *narrow pulse approximation*, i.e., assuming that no diffusion takes place during the gradient pulse ($\delta \rightarrow 0$), the relation between the measured signal attenuation $E(\mathbf{q}, \tau)$ and the EAP $P(\mathbf{r}; \tau)$ is given by a Fourier transform (Stejskal, 1965):

$$E(\mathbf{q}, \tau) = \int_{\mathbb{R}^3} P(\mathbf{R}; \tau) e^{-2\pi i \mathbf{q} \cdot \mathbf{R}} d\mathbf{R} \quad \text{with} \quad \mathbf{q} = \frac{\gamma \delta \mathbf{G}}{2\pi} \quad \text{and} \quad \tau = \Delta - \delta/3, \quad (2)$$

where $E(\mathbf{q}, \tau) = S(\mathbf{q}, \tau)/S_0$ with $S(\mathbf{q}, \tau)$ the measured signal at diffusion encoding position \mathbf{q} and diffusion time τ [s] and S_0 is the baseline image acquired without diffusion sensitization ($q = 0$). We denote $q = \|\mathbf{q}\|$ [mm⁻¹], $\mathbf{q} = q\mathbf{u}$ and $R = \|\mathbf{R}\|$ [mm], $\mathbf{R} = R\mathbf{r}$, where \mathbf{u} and \mathbf{r} are 3D unit vectors and $q, R \in \mathbb{R}^+$. The wave vector \mathbf{q} on the right side of Eq. (2) is related to pulse length δ [s], nuclear gyromagnetic ratio γ [s⁻¹T⁻¹] and the applied diffusion gradient vector $\mathbf{G} = G\mathbf{u}$ with $G = \|\mathbf{G}\|$ [T/mm] the gradient strength. From these parameters the b-value can be written as $b = G^2 \delta^2 \gamma^2 (\Delta - \delta/3)$ [s/mm²] (Le Bihan et al., 1986). Note that we write $P(\mathbf{R}; \tau)$ with a semicolon “;” as it describes a probability density over \mathbf{R} given τ .

The four-dimensional EAP has boundary conditions with respect to $\{\mathbf{q}, \tau\}$:

- $\{\mathbf{q} \in \mathbb{R}^3, \tau = 0\}$: When $\tau = 0$ the spins have no time to diffuse and the EAP is a spike function at the origin, i.e. $P(\mathbf{R}; \tau = 0) = \delta(\mathbf{R})$ with δ only here the Dirac delta function. Following Eq. (2), the signal attenuation will not attenuate for any value of \mathbf{q} , i.e., $E(\mathbf{q}, \tau = 0) = 1$.
- $\{\mathbf{q} \in \mathbb{R}^3, \tau \rightarrow \infty\}$: In the limit of infinite diffusion time only signal contributions from restricted compartments remain (Callaghan, 1995; Price, 1997). In this case, given infinite gradient strength and some assumptions on tissue composition, q-space indices such as the Return-To-Axis Probability (RTAP) are related to the mean apparent axon diameter (Özarslan et al., 2013b; Fick et al., 2016c).
- $\{\mathbf{q} = 0, \tau \in \mathbb{R}^+\}$: When there is no diffusion sensitization then $E(\mathbf{q} = 0, \tau) = 1$. With the Fourier relationship in Eq. (2), this point also corresponds to the zeroth harmonic of the EAP, which as a probability density integrates to one.
- $\{\mathbf{q} \rightarrow \infty, \tau \in \mathbb{R}^+\}$: In the limit of infinitely strong gradients even an infinitesimally small spin movement will attenuate the signal completely. This means that only trapped water particles still contribute to the signal attenuation. In *ex-vivo* tissues, a significant signal contribution of trapped water has been found (Alexander et al., 2010), meaning $\lim_{\mathbf{q} \rightarrow \infty} E(\mathbf{q}, \tau) = f_{\text{trapped}}$ with f_{trapped} the trapped water volume fraction. In *in-vivo* tissues, this contribution has been found to be negligible (Veraart et al., 2016), meaning $\lim_{\mathbf{q} \rightarrow \infty} E(\mathbf{q}, \tau) = 0$.

2.3. $q\tau$ -Signal Representation

In dMRI, functional basis approaches have been used to efficiently represent the diffusion signal with little assumptions on its shape. Following this methodology, we represent the measured $q\tau$ -signal attenuation $E(\mathbf{q}, \tau)$ in terms of a continuous functional basis $\hat{E}(\mathbf{q}, \tau; \mathbf{c})$, where the signal is now represented in terms of coefficients $\mathbf{c} \in \mathbb{R}^{N_c}$ with N_c the number of coefficients. An effective representation $\hat{E}(\mathbf{q}, \tau; \mathbf{c})$ should be able to

1. closely approximate the measured $q\tau$ -signal attenuation,
2. smoothly interpolate between and outside the measured $\{\mathbf{q}, \tau\}$ points,
3. have a sparse representation in \mathbf{c} ,
4. and be able to reconstruct the EAP from the fitted signal.

Requirements 1–3 are described in Eq. (3) such that

$$\begin{aligned} & \underbrace{\iint [E(\mathbf{q}, \tau) - \hat{E}(\mathbf{q}, \tau; \mathbf{c})]^2 d\mathbf{q}d\tau}_{(1) \text{ Data Fidelity}} + \lambda \underbrace{\iint [\nabla_{\mathbf{q}\tau}^2 \hat{E}(\mathbf{q}, \tau; \mathbf{c})]^2 d\mathbf{q}d\tau}_{(2) \text{ Smoothness}} + \underbrace{\alpha \|\mathbf{c}\|_1}_{(3) \text{ Sparsity}} \\ & \text{subject to } E(0, \tau; \mathbf{c}) = 1, E(\mathbf{q}, 0; \mathbf{c}) = 1 \end{aligned} \quad (3)$$

with λ and α regularization weights. Note that the integrals over \mathbf{q} have limits $[-\infty, \infty]$ and those over τ have limits $[0, \infty]$. As stated in Section 2.2, the boundary constraints are important to respect the Fourier relationship between the fitted signal attenuation and the EAP.

The Fourier relationship, shown above as the fourth condition, follows from our choice of a functional basis that is also a *Fourier* basis. More formally, by choosing a Fourier basis, the following condition is met:

$$\hat{P}(\mathbf{R}; \tau, \mathbf{c}) = \text{IFT}_{\mathbf{q}} \left[\hat{E}(\mathbf{q}, \tau; \mathbf{c}) \right]. \quad (4)$$

This means that once the coefficients \mathbf{c} are fitted we immediately also obtain the EAP representation.

2.3.1. Functional Basis Signal Representation

We represent the $q\tau$ -signal using an orthogonal basis that allows for the implementation of all our previously stated requirements. As we assume the narrow pulse approximation ($\delta \rightarrow 0$), we draw inspiration from Callaghan’s (1995) description of time-dependent diffusion in pores, and represent the dependence of the dMRI signal to \mathbf{q} and τ with two independent functions. We represent the combined space $\hat{E}(\mathbf{q}, \tau; \mathbf{c})$ using the cross-product between the spatial basis $\Phi(\mathbf{q})$ and temporal basis $T(\tau)$ as

$$\hat{E}(\mathbf{q}, \tau; \mathbf{c}) = \sum_i^{N_{\mathbf{q}}} \sum_k^{N_{\tau}} \mathbf{c}_{ik} \Phi_i(\mathbf{q}) T_k(\tau), \quad (5)$$

where $N_{\mathbf{q}}$ and N_{τ} are the maximum expansion orders of each basis and \mathbf{c}_{ik} weights the contribution of the ik^{th} basis function to $\hat{E}(\mathbf{q}, \tau; \mathbf{c})$.

A plethora of functional bases to represent \mathbf{q} have been proposed, (Descoteaux et al., 2007; Assemblal et al., 2009; Descoteaux et al., 2011; Caruyer and Deriche, 2012; Merlet and Deriche, 2013; Rathi et al., 2014; Özarslan et al., 2013a,b; Hosseinbor et al., 2013). Of these bases, we use the Mean Apparent Propagator (MAP) basis (Özarslan et al., 2013b) as it neatly fulfills all four previously stated requirements; (1) being an orthogonal basis, it can accurately represent any signal over \mathbf{q} using few coefficients; (2) it allows to impose smoothness using analytic Laplacian regularization (Fick et al., 2016c); (3) the isotropic MAP implementation was previously used to obtain sparse signal representation (Merlet and Deriche, 2013) and (4) MAP is a Fourier basis.

MAP's signal basis is a product of three orthogonal Simple Harmonic Oscillator-based Reconstruction and Estimation (SHORE) functions $\phi_n(u)$ (Özarslan et al., 2011):

$$\begin{aligned}\Phi_{N(i)}(\mathbf{q}, \mathbf{A}) &= \phi_{n_1}(q_x, u_x)\phi_{n_2}(q_y, u_y)\phi_{n_3}(q_z, u_z) \\ \text{with } \phi_n(q, u) &= \frac{i^{-n}}{\sqrt{2^n n!}} e^{-2\pi^2 q^2 u^2} H_n(2\pi u q)\end{aligned}\tag{6}$$

with its Fourier transform, the EAP basis as

$$\begin{aligned}\Psi_{N(i)}(\mathbf{R}, \mathbf{A}) &= \psi_{n_1}(R_x, u_x)\psi_{n_2}(R_y, u_y)\psi_{n_3}(R_z, u_z) \\ \text{with } \psi_n(R, u) &= \frac{1}{\sqrt{2^{n+1}\pi n!}u} e^{-R^2/(2u^2)} H_n(R/u)\end{aligned}\tag{7}$$

where H is a physicist's Hermite polynomial of order n , u is a data-dependent scale factor, $\Phi = FT(\Psi)$ and $\phi = FT(\psi)$. As in MAP (Özarslan et al., 2013b), before fitting, the data is rotated such that the DTI eigenvectors are aligned with the coordinate axis and we can use the data-dependent scaling matrix $\mathbf{A} = \text{Diag}(u_x^2, u_y^2, u_z^2)$ to scale the MAP basis functions according to the anisotropy of the data. As we show on the left of Figure 3, the zeroth order is a purely Gaussian function while higher orders use the oscillating Hermite polynomials to represent non-Gaussian aspects of the signal. For a given radial order N_{rad} the number of coefficients is $N_{\mathbf{q}} = (N_{\text{rad}} + 2)(N_{\text{rad}} + 4)(2N_{\text{rad}} + 3)/24$.

As limiting cases, the τ -dependence of the diffusion signal is exponential for pure Gaussian diffusion and constant for diffusion in restricted geometries (Callaghan, 1995). An appropriate functional basis to represent the signal over τ should therefore be able to represent signal profiles between these two boundary cases with relatively few coefficients. We chose to use a product of the negative exponential and a Laguerre polynomial L_p , which together form an orthogonal basis over τ , as it can quickly capture the negative exponential nature of the temporal diffusion signal. The temporal basis is given as

$$T_p(\tau, u_t) = \exp(-u_t\tau/2)L_p(u_t\tau)\tag{8}$$

with basis order p and temporal scaling factor u_t . As we show in the right of Figure 3, the zeroth order is a pure exponential function and higher orders use the oscillating Laguerre polynomials to represent non-exponential aspects of the signal. Given enough coefficients, this time basis is able to represent any temporal diffusion signal without making assumptions on the underlying tissue structure. We study how many coefficients we actually need to represent the complete $q\tau$ -signal in Section 4.

[Figure 3 about here.]

For the rest of this work we will linearize the ordering of our $q\tau$ -basis such that we use one basis index i with notation

$$\hat{E}(\mathbf{q}, \tau; \mathbf{c}) = \sum_i^{N_c} \mathbf{c}_i \Xi_i(\mathbf{q}, \tau, \mathbf{A}, u_t) = \sum_i^{N_c} \mathbf{c}_i \Phi_{N(i)}(\mathbf{q}, \mathbf{A}) T_{p(i)}(\tau, u_t)\tag{9}$$

where the total number of fitted coefficients is $N_c = (N_\tau + 1)(N_{\text{rad}} + 2)(N_{\text{rad}} + 4)(2N_{\text{rad}} + 3)/24$.

The $q\tau$ -EAP can be reconstructed using MAP's Fourier properties (Özarslan et al., 2013b). The Fourier transform only concerns the \mathbf{q} -space, so the EAP is found simply by switching $\Phi(\mathbf{q}, \mathbf{A})$ in Eq. (9) by its Fourier transform $\Psi(\mathbf{R}, \mathbf{A})$ in Eq. (7).

2.3.2. Analytic Laplacian Regularization

We impose smoothness in the $q\tau$ -signal reconstruction by using the squared norm of the Laplacian of the reconstructed signal. In dMRI, this type of regularization has successfully been applied to several other techniques (Descoteaux et al., 2007; Caruyer and Deriche, 2012; Fick et al., 2016c). We define the *Smoothness* term in Eq. (3) as Laplacian functional $U(\mathbf{c})$ as

$$U(\mathbf{c}) = \iint \left[\nabla_{\mathbf{q}\tau}^2 \hat{E}(\mathbf{q}, \tau; \mathbf{c}) \right]^2 d\mathbf{q} d\tau \quad (10)$$

where, due to our choice of basis, the Laplacian of the reconstructed signal can be estimated as $\nabla_{\mathbf{q}\tau}^2 \hat{E}(\mathbf{q}, \tau; \mathbf{c}) = \sum_i c_i \nabla_{\mathbf{q}\tau}^2 \Xi_i(\mathbf{q}, \tau, \mathbf{A}, u_t)$. Eq. (10) can be further rewritten in quadratic form as $U(\mathbf{c}) = \mathbf{c}^T \mathbf{U} \mathbf{c}$ with elements

$$\mathbf{U}_{ik} = \iint \nabla_{\mathbf{q}\tau}^2 \Xi_i(\mathbf{q}, \tau, \mathbf{A}, u_t) \cdot \nabla_{\mathbf{q}\tau}^2 \Xi_k(\mathbf{q}, \tau, \mathbf{A}, u_t) d\mathbf{q} d\tau \quad (11)$$

where the subscript ik indicates the ik^{th} position in the regularization matrix. We use the orthogonality of the basis functions (standard inner product on $[0, \infty]$) to compute the values of the regularization matrix to a closed form depending only on the basis orders and scale factors. For brevity here, we provide the formulation of \mathbf{U} in Appendix B.

2.3.3. Coefficient Estimation from $q\tau$ -Signal

We represent the $q\tau$ -signal $E(\mathbf{q}, \tau)$ in terms of a sparse coefficient vector \mathbf{c} as $\mathbf{y} = \mathbf{Q}\mathbf{c} + \epsilon$ where $\mathbf{y} \in \mathbb{R}^{N_y}$ are the signal values with N_y the number of samples, $\mathbf{Q} \in \mathbb{R}^{N_y \times N_c}$ the observation matrix with elements $\mathbf{Q}_{ij} = \Xi_j(\mathbf{q}_i, \tau_i, \mathbf{A}, u_t)$ and $\epsilon \in \mathbb{R}^{N_y}$ the acquisition noise. We frame the numerical implementation of our approach in the same way as we did continuously in Eq. (3):

$$\begin{aligned} & \underset{\mathbf{c}}{\operatorname{argmin}} \quad \overbrace{\|\mathbf{y} - \mathbf{Q}\mathbf{c}\|_2^2}^{(1) \text{ Data Fidelity}} + \overbrace{\lambda \|\mathbf{c}^T \mathbf{U} \mathbf{c}\|_2^2}^{(2) \text{ Smoothness}} + \overbrace{\alpha \|\mathbf{c}\|_1}^{(3) \text{ Sparsity}} \\ & \text{subject to } \mathbf{Q}^{\{\mathbf{q}=0, \tau \in \mathbb{R}^+\}} \mathbf{c} = \mathbf{1} \end{aligned} \quad (12)$$

where we described the *Smoothness* term in Section 2.3.2. The *Sparsity* term and constraints are imposed by framing our problem as a convex optimization using the open-source package CVXPY (Diamond and Boyd, 2016). Note that we only impose the first $E(\mathbf{q} = 0, \tau; \mathbf{c})$ constraint as this is the only one that influences $q\tau$ -index estimation. The second $E(\mathbf{q}, \tau = 0; \mathbf{c})$ constraint is irrelevant as no diffusion takes place when $\tau = 0$. We find optimal values for regularization weights α and λ using cross-validation and implemented the surrounding code infrastructure inside the DiPy framework (Garyfallidis et al., 2014). In fact, the entire $q\tau$ -dMRI framework for regularized coefficient and $q\tau$ -index estimation will shortly be available at <http://nipy.org/dipy/>. We provide the detailed fitting procedure in Appendix A.

2.4. Estimation of $q\tau$ -Indices

Once coefficients \mathbf{c} are known, our basis allows us to freely explore, for any diffusion time, all previously proposed scalar metrics for the three-dimensional EAP (Özarslan et al., 2013b; Fick et al., 2016c), also known as \mathbf{q} -space indices. We can do this because our basis reduces to the MAP basis when the temporal basis is evaluated for a particular diffusion time. In this work, we illustrate this

using the τ -dependent Return-To-Origin Probability (RTOP) (Hürlimann et al., 1995), Return-To-Axis Probability (RTAP), Return-To-Plane Probability (RTPP) and Mean Squared Displacement (MSD). We will refer to these time-dependent q-space indices as $q\tau$ -indices.

As the name implies, the MSD describes the average squared distance that particles travel given τ , and can be estimated from the EAP as

$$\text{MSD}(\tau) \triangleq \int_{\mathbb{R}} \int_{\mathbb{S}^2} P(R\mathbf{r}; \tau) R^2 d\mathbf{r} dR. \quad (13)$$

The RTOP describes the probability density that particles start and end at the same position after τ . While MSD and RTOP are rotationally invariant features, RTAP and RTPP are *directional* scalar indices that assume the white matter tissue is modeled by parallel cylinders, with \mathbf{r}_{\parallel} parallel and \mathbf{r}_{\perp} perpendicular to the cylinder axis. This assumption is needed to interpret RTAP and RTPP as features of the diffusion signal parallel to cylinder axis, or the perpendicular cylinder plane, respectively. In practice, the underlying tissue always deviated from this assumption due to axon dispersion, which is present even in the most coherent white matter bundles (Leergaard et al., 2010; Ronen et al., 2014). While axon dispersion does bias the estimation of q- and $q\tau$ -space indices (Fick et al., 2016a; Zucchelli et al., 2016), we can still regard RTAP and RTPP as being directional with respect to the principal bundle axis. The indices are formulated as

$$\begin{aligned} \text{RTOP}(\tau) [\text{mm}^{-3}] &\triangleq P(0; \tau), \\ \text{RTAP}(\tau) [\text{mm}^{-2}] &\triangleq \int_{\mathbb{R}} P(R\mathbf{r}_{\parallel}; \tau) dR, \\ \text{RTPP}(\tau) [\text{mm}^{-1}] &\triangleq \int_{\mathbb{R}} \int_{\{\mathbf{r} \in \mathbb{S}^2 : \mathbf{r} \cdot \mathbf{r}_{\parallel} = 0\}} P(R\mathbf{r}_{\perp}; \tau) d\mathbf{r}_{\perp} dR. \end{aligned} \quad (14)$$

We refer to these time-dependent q-space index functions as $q\tau$ -indices for brevity. We note that the estimation of $q\tau$ -indices is dependent on the included diffusion times τ and strongest diffusion sensitization q_{\max} of the acquisition scheme. An acquisition scheme should not have different q_{\max} for different τ , as is illustrated in Figure 4. If not, estimated $q\tau$ -indices describe changes in the acquisition scheme instead of the tissue. To give intuition on this, our $q\tau$ -dMRI basis can fit any $q\tau$ -space signal up to q_{\max} for every τ , after which the signal representation will smoothly attenuate to zero. If q_{\max} is the same for every τ , then this attenuation will start at the same q-point for every τ , and changes in estimated $q\tau$ -space indices over τ will actually reflect temporal changes in the diffusion signal up to q_{\max} . Small variations in q_{\max} over τ can be compensated for by $q\tau$ -dMRI’s smooth interpolation between $q\tau$ -points, but for larger q_{\max} variations the temporal interpretation of $q\tau$ -indices becomes increasingly complicated.

3. Data Set Specification

3.1. $q\tau$ -Acquisition Scheme design and in-vivo Mouse Data Specifics

An illustration of our acquisition scheme is given in Figure 4. We acquire 35 different “shells” with 21 uniformly spread DWIs and one b_0 each using pulse duration $\delta = 5\text{ms}$, resulting in 770 DWIs in the simulated data. Over these shells, we measure five equispaced “ τ -shells” $\Delta = \{10.8, 13.1, 15.4, 17.7, 20\}\text{ms}$ and seven approximately equispaced “gradient shells” between $G = \{50 - 490\}\text{mT/m}$. Note that by keeping δ and G_{\max} the same over Δ we ensure that q_{\max}

does not change over τ , as we state is required in the previous section. The minimum b-value is $b_{\min} = 48\text{s}/\text{mm}^2$ and maximum b-value is $b_{\max} = 7814\text{s}/\text{mm}^2$. To uniformly spread DWIs in this four-dimensional acquisition scheme, we used the approach of Caruyer et al. (2013) to find an optimal sampling for one diffusion time and copied this scheme for every Δ .

As for the *in-vivo* acquisition, we acquired test-retest spin echo sequences from three C57Bl6 wild-type mice on an 11.7 Tesla Bruker scanner. The test and retest acquisition were taken 48 hours from each other. The data consists of $96 \times 160 \times 12$ voxels of size $110 \times 110 \times 500 \mu\text{m}$. For the well-being of the *in-vivo* subjects, we subsampled the synthetic scheme to a total of 580 DWIs also using the approach of Caruyer et al. (2013). Unfortunately, we had to discard the data of one of the subjects due to artifacts in the test acquisition. We manually created a brain mask and corrected the data from eddy currents and motion artifacts using FSL’s eddy (Andersson and Sotiropoulos, 2016). We then drew a region of interest in the middle slice in the corpus callosum, see Figure 4, where the tissue is reasonably coherent.

[Figure 4 about here.]

3.2. In Silico Data Sets with Camino

We use Camino (Cook et al., 2006) to reproduce diffusion signals originating from tissues containing realistic axon diameter distributions and packings. As we illustrate in Table 1, we use 5 gamma distributions from Aboitiz et al. (1992) and 6 from Lamantia and Rakic (1990). Like Alexander et al. (2010), we simulate the overall diffusion signal from these 11 distributions from the same distributions with doubled axonal diameters and two different packing densities, resulting in a total of 44 distributions. As simulations parameters, we used 100,000 walkers with 1000 time steps using a diffusivity of $1.7 \times 10^{-9}\text{m}^2/\text{s}$.

[Table 1 about here.]

4. Experiments and Results

4.1. Basis Order Selection and Method Comparison

$q\tau$ -dMRI uses a separate basis expansion over \mathbf{q} and τ , so it is important to determine the optimal (minimum) spatial and temporal basis order we need to accurately represent the $q\tau$ -signal. To do this we generate both Gaussian phantom data using realistic eigenvalues of $\{1.7, 1.2, 1.2\} \times 10^{-9}\text{m}^2/\text{s}$ and Camino-generated data from Section 3.2 using the $q\tau$ -acquisition scheme in Figure 4. In this noiseless experiment, we fit both data sets with increasing radial and temporal order and determine the mean squared error (MSE) of the fitted points themselves. We show the results in Figure 5a, where the color illustrates the mean MSE and the green dots illustrate order combinations where the mean absolute error is less than 1% of the b_0 -intensity. The Gaussian data can be accurately represented using only 21 coefficients using a radial and temporal order of 2. Representing the more realistic Camino data, which exhibits diffusion restriction over both \mathbf{q} and τ , takes at least 150 coefficients using a radial order of 6 and temporal order of 2. We will use this basis order combination in the rest of our experiments as this is the minimum number of coefficients to fit any $q\tau$ -signal.

We also compare the noiseless fitting error of our approach with that of DTI (Basser et al., 1994) and our previously proposed technique using 3D-SHORE as a spatial basis (Fick et al., 2015a) in Figure 5b. We use the same radial and temporal order of 6/2 for the 3D-SHORE-based and our

q τ -dMRI approach, both estimating 150 coefficients. We fit the Camino data while truncating at different maximum b-values and compute the MSE. We can see that DTI has a higher MSE compared to both other techniques, and that the MSE increases as higher b-value data is added. This shows that a simple Gaussian approximation cannot accurately represent the non-Gaussian aspects of the Camino phantom data at any b-value, which are more present at higher b-values. As for the approach by Fick et al. (2015a), its MSE starts at the same point as that of q τ -dMRI, but increases as the maximum b-value is increased. This is because it uses the isotropic 3D-SHORE basis as the spatial basis, which means it is less effective to fit the anisotropic diffusion signal, especially at higher b-values (Fick et al., 2016c). As expected, our q τ -dMRI approach, using the anisotropic MAP-MRI implementation, manages to keep an almost stable MSE over increasing maximum b-value.

[Figure 5 about here.]

To study to what extent higher order basis orders are being used in the reconstruction of the DTI and Camino phantoms using the chosen radial/temporal order of 6/2, we study the normalized spectral density of the q τ -dMRI coefficients per radial and temporal order. To suppress oscillations in the signal extrapolation that would express themselves in the highest order coefficients, we only used a very small Laplacian regularization weight $\lambda = 10^{-5}$ when estimating the coefficients. Since the q τ -space signal integral of each basis function in the q τ -dMRI basis is the same, we can estimate the normalized spectral density $\bar{\rho}_{\mathbf{c}}$ for a given radial order $N_{\mathbf{q}}$ and temporal order N_{τ} by only considering the coefficients \mathbf{c} . We estimate $\bar{\rho}_{\mathbf{c}}$ by taking the squared sum of the coefficients belonging to a radial and temporal order, and then divide it by the total squared sum of the spectrum:

$$\bar{\rho}_{\mathbf{c}}(N_{\mathbf{q}}, N_{\tau}) = \frac{\sum_{i=0}^{N_{\text{coef}}} c_{n_1 n_2 n_3 p(i)}^2 \delta(n_1(i) + n_2(i) + n_3(i), N_{\mathbf{q}}) \delta(p(i), N_{\tau})}{\sum_{i=0}^{N_{\text{coef}}} c_{n_1 n_2 n_3 p(i)}^2}. \quad (15)$$

Here i iterates over the spatial and temporal basis orders for all coefficients, and $\delta(\cdot, \cdot)$ is the Kronecker delta function, which is only non-zero when its two arguments are equal.

In Figure 6 we show the estimated spectral densities. We see that the densities for both phantoms is most concentrated in radial/temporal order of 0/0, after which the density decreases when either time or radial order is increased. In the Camino phantom there is still quite some density in the time order=1 coefficients, but the density significantly decreases for time order=2. The spectrum increase from radial order 2 to 4 for time order 1 is possibly because those basis functions are better suited for the data, but has no further meaning. For the DTI data there is much less density in the time order=1,2 coefficients compared to the Camino data, explaining why it is better fitted using lower orders in Figure 5a. In fact, in both phantoms many of the higher order coefficients are close to zero: 99% of the spectrum density of the Camino and DTI phantoms is concentrated in 32 and 19 coefficients, respectively. Of course, adding more coefficients to the fitting will allow us to even more closely approximate the data, but our choice of using a radial/temporal order of 6/2 seems to be a good trade-off between accuracy and efficiency.

[Figure 6 about here.]

4.2. Effectiveness of q τ -dMRI Regularization

To reduce the number of required measurements to represent the q τ -space, we regularize the fitting of q τ -dMRI using a combination of imposing signal smoothness and sparsity in the basis

coefficients. To study its effectiveness of this approach, we first add Rician noise to the Camino data such that the signal-to-noise (SNR)-ratio is 10, 20 and 30. We then randomly subsample the data such that we only fit between 490 and 40 DWIs. We estimate the fitting error by predicting the missing data points from the fitted representation and comparing them to the noiseless data. The experiment, for every chosen number of samples, is repeated 50 times for all 44 voxels with each a different noise instance. We show the results in Figure 7. Overall, the lower the SNR the higher the MSE for every technique. In all cases using least squares (red) results in by far the highest MSE. Using only Laplacian (green) already stabilizes the MSE much better. Using both Laplacian and ℓ_1 (yellow) produces the best results with the lowest MSE, especially at a lower number of samples.

[Figure 7 about here.]

4.3. Effect of Subsampling on the Estimation of $q\tau$ -Indices

Now that we have shown that our regularization allows us to use fewer measurements while keeping the fitting error low, we study the effect of subsampling on the estimation of $q\tau$ -indices. In Figure, 8 we show the estimated MSD, RTOP, RTAP and RTPP using between 600 DWIs (green) and 100 (blue) DWIs. Notice that, as expected, MSD increases and the return probabilities decrease as diffusion time increases. Also notice that $RTAP^{1/2} > RTOP^{1/3} > RTPP$ as the diffusion signal is more restricted perpendicular to the axon axis than parallel to it, and that the slopes of all indices go closer to zero as time increases. We used the square and cube root of RTAP and RTOP to put them in the same unit as RTPP. The estimation of the MSD appears stable to subsampling down to 200 DWIs, after which its profile becomes flat. On the other hand, the estimation of the return probabilities appears sensitive to subsampling and their value decreases as fewer DWIs are used in the fitting, with the exception of RTPP. We discuss this phenomenon in section 5.

[Figure 8 about here.]

4.4. Reproducibility on in-vivo Mouse Test-Retest Acquisition

Finally, we study the reproducibility of our method on *in-vivo* test-retest diffusion spin echo acquisitions of two C57Bl6 wild-type mice. We show a sagittal cross-section of the fractional anisotropy (FA) map of the four data sets and the acquisition scheme in Figure 4. We drew a region of interest in the corpus callosum of each data set for our experiments.

As in the synthetic experiments, we first study the fitting error while randomly subsampling the data. We show the MSE per subject for both test and retest acquisitions in Figure 9. As before, we find that using our combined Laplacian and ℓ_1 regularization reduces the MSE significantly. Notice that we broke the y-axis in half because we had to use log-scale to accurately depict the least squared MSE, which can indeed go up to 10^{10} . Also notice that the MSE between the test-retest and between subjects is very similar.

[Figure 9 about here.]

Using the full data, we then estimate the $q\tau$ -indices for the test-retest (red-green) of all subjects and show the results in Figure 10. In agreement with the synthetic experiments, we again find that MSD increases and the return probabilities decrease over diffusion time and $RTAP^{1/2} > RTOP^{1/3} > RTPP$. Subject 1 shows that, for all indices, the mean retest indices fall within 0.2 standard deviations of the test indices with similar dispersion. Subject 2 shows similar overlap for the q-space indices, but the retest MSD is slightly off.

The gray isolines in the background represent the index values for free diffusion with a range of diffusion coefficients, as shown in the color bar. For every index, we annotated the isolines in between which the values of that index range. In this way, it becomes easier to see that all indices describe a diffusion process that is slower than Gaussian. For example, in the top-left graph, the estimated MSD starts at the shortest diffusion time around free diffusion coefficient $D = 12 \times 10^{-4} \text{mm/s}^2$ and ends at the longest diffusion time at $D = 10 \times 10^4 \text{mm/s}^2$; an observed reduction of $2 \times 10^{-4} \text{mm/s}^2$. This trend holds for most indices, but the corresponding values for the diffusion coefficient varies per index. For example, the observed diffusion coefficient for RTPP is much higher than that of RTAP, because they describe diffusion parallel and perpendicular to the bundle axis, respectively. By extension, RTOP, a rotation invariant feature describing the overall diffusion process, lies in between RTAP and RTPP.

[Figure 10 about here.]

To better illustrate the deviation from Gaussian decay, we visualize the mean MSD and return probabilities of both Test subjects in a log-log plot in Figure 11. Power-laws of the form $y = ax^k$ show as straight lines in log-log plots, meaning Gaussian diffusion will always have the same slope no matter the diffusivity. Note that estimating temporal power law coefficients of $q\tau$ -indices have no physical or microstructural interpretation (Novikov et al., 2016), but this experiment serves to illustrate the non-Gaussian aspects of the diffusion process for finite τ , which can be quantified using our $q\tau$ -dMRI approach.

On the top, we see that the MSD starts close-to-Gaussian, but becomes more restricted as time increases. On the bottom, we see that RTPP, describing parallel diffusion, is almost completely Gaussian over diffusion time – as expected in such coherent white matter. On the other hand, RTAP is non-Gaussian from the start, and RTOP again lies in between RTAP and RTPP. Recalling Section 2.2, it should be noted that the time-dependence of $q\tau$ -indices should become flat because only signal contributions from restricted compartments will remain in the long diffusion time regime (Novikov et al., 2016).

[Figure 11 about here.]

5. Discussion

In the early days of diffusion MRI, diffusion time dependence was initially explored to probe diffusion restriction in brain tissues (Moonen et al., 1991; Le Bihan et al., 1993; Le Bihan, 1995; Assaf et al., 1998). Though, once the the concept of diffusion restriction was established (Beaulieu, 2002), the focus of the community shifted towards estimation of the angular features of the diffusion process (Tuch, 2004; Tournier et al., 2007; Descoteaux et al., 2007; Aganj et al., 2010). Only recently has the community refocused on the exploration of the τ -dependence of the dMRI signal (Assaf et al., 2004, 2008; Pyatigorskaya et al., 2014; Novikov et al., 2014; Burcaw et al., 2015; De Santis et al., 2016; Fieremans et al., 2016; Ning et al., 2016; Ferizi et al., 2016; Palombo et al., 2016). To allow non-parametric exploration of diffusion τ -dependence, we proposed a functional basis approach that we call $q\tau$ -dMRI. Our approach facilitates the estimation of τ -dependent q -space indices ($q\tau$ -indices), which provide quantitative characterization of τ -dependence. In this section, we discuss the results of our experiments in Section 5.1, considerations about the formulation of $q\tau$ -dMRI in Section 5.2 and future perspectives in Section 5.3.

5.1. Discussion of the results and interpretation of $q\tau$ -indices

In this section, we focus on the interpretation of the results we presented in Section 4.

$q\tau$ -dMRI effectively describes the τ -dependence of the diffusion signal at finite τ :

We studied how many coefficients $q\tau$ -dMRI needs to accurately represent both restricted and free $q\tau$ -signals for a finite τ -range. In Figure 5a, we showed that to represent the diffusion signal in anisotropic white matter we needed at least 150 coefficients, using a radial/temporal order of 6/2. Using lower basis orders would cause bias in the signal reconstruction since the model will become too simple for the data: the MSD would probably still increase and RTOP/RTAP/RTPP would still decrease over τ , but these trends would likely not describe the nature of the fitted data very well. During a previous study on q -space index estimation we found that using a too low radial order often results in an overestimation of RTAP (Fick et al., 2015b). On the other hand, increasing the basis orders further will allow the basis to fit even more complex signals, but regularization of the basis in the presence of noise would become increasingly difficult and time-consuming. We chose the orders 6/2 to have a good trade-off between accuracy and efficiency of fitting white matter data. Furthermore, while our basis does not include a Gaussian compartment – since a Gaussian $\exp(-q^2\mathbf{D}\tau)$ cannot be exactly rewritten in terms of our spatial basis $\exp(-2\pi^2q^2\mathbf{A})$ and temporal basis $\exp(-u_t\tau/2)$ – we can closely approximate any Gaussian signal using only 21 coefficients. In Figure 5b, we also showed that $q\tau$ -dMRI’s fitting error is lower than our previously proposed 3D+t approach (Fick et al., 2015a) and DTI (Basser et al., 1994). The main methodological advances of $q\tau$ -dMRI over 3D+t are its \mathbf{q} -space representation, where we use the MAP basis instead of 3D-SHORE, the sparsity term, and the explicit boundary constraints at $\tilde{E}(\mathbf{q} = 0, \tau; \mathbf{c}) = 1$. The added value of these advances becomes more apparent at higher b-values, where the diffusion signal is most characterizing of the underlying tissue. We remark that DTI is inherently limited to describe temporal diffusion restriction because its propagator of the form $\exp(-q^2D(\tau)\tau)$ can only measure the diffusion coefficient for one particular τ . The τ -dependence of $D(\tau)$ means there must be higher-order cumulants (e.g. kurtosis) that DTI cannot accurately represent (Novikov and Kiselev, 2010). This is illustrated by the observed non-Gaussian behavior at finite diffusion time in Figure 11. With respect to alternative multi-compartment $q\tau$ -approaches, in Fick et al. (2015a), we compared our previous 3D+t model with CHARMED (Assaf et al., 2004) and found that our functional basis approach reconstructed a less biased representation of the $q\tau$ -space. Hence, as the approach in this paper improves upon 3D+t, the same is true for $q\tau$ -dMRI. Lastly, by estimating the coefficient spectrum density in Figure 6 we also showed that most of the signal information is stored in relatively few coefficients, and most is concentrated in the lower basis orders.

$q\tau$ -dMRI facilitates estimation of $q\tau$ -indices: In previous studies, $q\tau$ -indices were studied in an *ex-vivo* setting using voxel-wise “AxCaliber”-style acquisitions, varying only over \mathbf{q} and τ in one preset direction (Özarslan et al., 2006, 2012). However, the practical application of this approach is limited when the tissue orientation is not known beforehand. Our work transcends this limitation in allowing the estimation of $q\tau$ -indices in a four-dimensional setting (3D q -space and diffusion time). For any evaluated diffusion time $q\tau$ -dMRI reduces to MAP. This allows us to calculate any previously proposed EAP feature such as MSD or RTOP (Özarslan et al., 2013b; Fick et al., 2016c).

Physiological interpretation of $q\tau$ -indices: $q\tau$ -indices are signal-based properties, making no distinction between intra- or extra-axonal signal contributions. For realistic axon diameters ($< 2\mu\text{m}$) (Aboitiz et al., 1992), the diffusion perpendicular to the axon axis is likely already restricted before τ_{\min} of the acquisition (Assaf et al., 2008). If this is true, then the changes we observe in $q\tau$ -indices over τ , in particular RTAP, must originate from the extra-axonal space exclusively.

The slope of RTAP over τ could, therefore, describe packing properties of the axons. This is also the focus of recent studies on the extra-axonal space (Novikov et al., 2014; Burcaw et al., 2015). However, exchange between the intra-axonal and extra-axonal space could also influence the slopes of these indices (Fieremans et al., 2010), although no agreement has been reached on the true permeability of axonal membranes (See e.g. Lätt et al., 2009; Quirk et al., 2003), and whether or not it can be neglected at high diffusion times. $q\tau$ -indices also still depend on the narrow pulse approximation ($\delta \rightarrow 0$), so its actual choice should be kept in mind in studying $q\tau$ -indices as they do influence their values (Bar-Shir et al., 2008). Finally, the often non-Gaussian nature of the acquisition noise biases the estimation of q -space indices (Avram et al., 2015). This bias could be reduced through multi-shell signal denoising (Manjón et al., 2013; St-Jean et al., 2016) or phase correction (Pizzolato et al., 2016) strategies.

Combined Laplacian and ℓ_1 regularization provides robustness to noise and subsampling: We compared the fitting error of our combined regularization strategy with that of other regularization approaches. In Figure 8, we showed that imposing both signal smoothness through Laplacian regularization and signal sparsity using the ℓ_1 -norm produces the lowest fitting error for any number of samples. Using only Laplacian regularization as in Fick et al. (2015a) produces higher fitting errors when fewer than 200 samples are fitted, but performs similarly otherwise. Our combined regularization scheme can be seen as a modification to Elastic-Net regularization (Zou and Hastie, 2005) along the same lines as GraphNet (Grosenick et al., 2013). Similar to their approach, we modify ℓ_2 -norm penalty term in the Elastic-Net to use the norm of the Laplacian of the measured signal. Our approach differs from theirs in that the coefficients in $q\tau$ -dMRI represent the Eigenfunctions of the signal and EAP, while those of GraphNet are discrete measurements of graph connectivity. This allows for the closed-form estimation of the Laplacian in the $q\tau$ -space, as we illustrate in Appendix B.

Estimated $q\tau$ -index trends are consistent and robust to subsampling: In Figure 8, we show that we obtain the expected index trends over diffusion time, where on simulated data the MSD increases and the return probabilities decrease as diffusion time increases. Regarding MSD, we found that its estimation is relatively unaffected by subsampling. This is expected as MSD is a function of the bulk motion of the EAP (see Eq. (13) and is estimated using the Laplacian of the signal attenuation at $E(\mathbf{q} = 0, \tau)$ (Cheng, 2014). Removing measurements at large \mathbf{q} therefore has little effect on its estimation. Figure 8 also shows that the estimation of return probabilities *is* sensitive to subsampling, but still produces consistently decreasing index slopes. This is a result of their dependency on q -space integrals until infinity (Özarslan et al., 2013b), meaning their values depends on signal extrapolation beyond the largest measured q -value. This induces specific behavior in $q\tau$ -index trends. When samples are removed along or close to the “restricted” perpendicular signal direction, the signal inter- and extrapolation will perceive a less restricted signal, leading to an underestimation of RTAP. Conversely, removing samples along the parallel direction will not influence RTPP as much as the perceived signal was already free. Finally, RTOP includes both RTAP and RTPP and therefore experiences a subsampling sensitivity between that of RTAP and RTPP. In agreement with Avram et al. (2015), this reasoning also explains why we consistently find that $RTAP^{1/2} > RTOP^{1/3} > RTPP$ (see Figures 8, 10 and 11); return probabilities increase as diffusion becomes more restricted. Overall, using the chosen basis orders, a lower bound of reliable index estimation seems to be around 200 samples using random subsampling, as all profiles flatten out at this point.

Estimation of $q\tau$ -indices is reproducible *in-vivo*: We tested the reproducibility of $q\tau$ -index estimation on two test-retest diffusion Spin Echo acquisitions of C57B16 wild-type mice. We

selected an ROI in the corpus callosum (Figure 4) to limit our study to anisotropic white matter with minimal axonal dispersion effects (Leergaard et al., 2010; Ronen et al., 2014). We acquired anisotropic voxels to improve the SNR at high gradient strengths and diffusion times. Fitting $q\tau$ -dMRI to the *in-vivo* data produced results that are in agreement with the synthetic experiments; both the fitting error and $q\tau$ -index trends are similar (Figures 9 and 10). Of particular interest is Figure 10, where we plot the test-retest values of MSD, RTAP, RTOP and RTPP over diffusion time. The isolines in the background, representing the q -space index value for free diffusion with varying diffusivity, shows that $q\tau$ -dMRI q -space trends are actually picking up on diffusion restriction over diffusion time. For different indices we find different levels of restriction over time. This is particularly clear in the log-log plots in Figure 11. In log-log plots, power-laws of the form $\text{Index}(\tau) \propto \tau^k$ show as straight lines with slope k . Gaussian diffusion will therefore always have the same slope regardless of the diffusivity. We can clearly see that the slope of RTPP the steepest and is nearly parallel to that of Gaussian diffusion, while the slope of RTAP is the shallowest, showing the most restriction.

5.2. Considerations on the formulation and implementation of $q\tau$ -dMRI

In this section, we discuss our considerations in implementing the $q\tau$ -dMRI framework. We implemented our approach by making use of the functionality inside the open-source Diffusion Imaging in Python (Dipy) software project for computational neuroanatomy (Garyfallidis et al., 2014). In fact, the entire $q\tau$ -dMRI framework for regularized coefficient and $q\tau$ -index estimation will shortly be available at <http://nipy.org/dipy/>.

On Choice of Functional Basis and Finite Diffusion Time: Our separable basis formulation allows us to independently choose any previously proposed functional basis to represent 3D q -space and diffusion time. Out of the numerous q -space representations that have been proposed (Descoteaux et al., 2007, 2011; Assemlal et al., 2009; Caruyer and Deriche, 2012; Özarslan et al., 2013a,b; Hosseinbor et al., 2013, 2015; Rathi et al., 2014; Cheng et al., 2015b) we chose the MAP basis (Özarslan et al., 2013b) for its convenient EAP reconstruction, wide range of q -space indices and closed-form Laplacian regularization (Fick et al., 2016c). To represent diffusion time for finite τ , based on studies by Callaghan (1995), we proposed a novel functional basis based on negative exponential decay. Our basis formulation allows for effective representation of the $q\tau$ -space at finite q and τ – without making biophysical assumptions. This means that the technique we introduce in this work can be used as a signal preprocessing step for subsequent parametric modeling of the $q\tau$ -space, as previously done with the 3D q -space (Fick et al., 2016c). Recent work by Veraart et al. (2016) suggests that at high $q\tau$ -values, oscillating basis functions are suboptimal representations. However, our results, shown in Section 4, show that at the $q\tau$ -values used in this study, much higher than those available in human scenarios, our approach is a useful tool to synthesize the $q\tau$ -dMRI signal.

On Sparsity: When imposing sparsity in the coefficient space, it is customary to ensure that the inner product of each basis function in the representation is unity such that $\iint \Xi_i(\mathbf{q}, \tau) \Xi_i(\mathbf{q}, \tau) d\mathbf{q} d\tau = 1$ (Candès et al., 2006). However, in practice it is sufficient that the inner product is *constant* for all basis functions. Since the inner product of our spatial MAP basis and our temporal basis only depends on the voxel-wise scale factors, we can effectively omit the basis normalization without affecting the sparsity constraint. However, to impose sparsity when the spatial representation is e.g. the 3D-SHORE basis (Fick et al., 2015a) we need to use appropriate basis function normalization. For completeness, we provide the derivation of the normalized basis functions and normalized Laplacian regularization in Appendix D.

On Smoothness: To impose smoothness using the four-dimensional Laplacian of the reconstructed signal, it is important that the scales of the 3D q -space and 1D diffusion time are in the same order. If not, the Laplacian will disproportionately regularize one space over the other. For this reason, the algorithm internally uses a scaled diffusion time $\tau^* = \tau \times (u_t/\tilde{u}_s)$ and scale factor $u_t^* = \tilde{u}_s$ with \tilde{u}_s the mean spatial scale factor. This rescaling does not affect any of the observation matrices that fit the signal, but only the relative weighting inside the Laplacian regularization functional in Eq. (10).

On Echo Time: Our basis describes the $q\tau$ -diffusion attenuation $E(\mathbf{q}, \tau) = S(\mathbf{q}, \tau)/S_0$, where the division by the S_0 intensity normalizes for the Echo Time (TE) of the acquisition. However, to optimize an acquisition for SNR it is often customary to reduce the TE as much as possible for a given diffusion time. While we avoided doing so in our work, it is possible to fit our $q\tau$ -dMRI approach to data that uses multiple TE by normalizing the different TE segments *separately* and concatenating the normalized data afterward. Another approach is to normalize the different TE segments together using T_2 estimation, but it should be noted that T_2 estimation is not trivial (Milford et al., 2015).

On Signal Extrapolation: While our choice of spatial and temporal choice of bases is efficient in fitting the $q\tau$ -signal and allows for convenient closed-form regularization, there are some inherent limitations to our choice as well. It is well-known that the diffusion signal over τ within restricted media, assuming no significant exchange is present, does not attenuate to zero as $\lim_{\tau \rightarrow \infty}$ but finds some plateau value (Price, 1997). Since our basis consists of decaying oscillating functions our representation will always smoothly attenuate to zero after the last fitted data point such that $\lim_{\mathbf{q} \rightarrow \infty} \hat{E}(\mathbf{q}, \tau) \equiv \lim_{\tau \rightarrow \infty} \hat{E}(\mathbf{q}, \tau) \equiv 0$. It is possible to overcome this limitation by adding an infinite time component in our basis fitting, but this would be at the cost of having closed-form Laplacian regularization of the $q\tau$ -signal.

On Boundary Conditions: As our basis consists of oscillating functions, constraints must be put in place to adhere to the boundary cases of the $q\tau$ -signal at $\hat{E}(\mathbf{q} = 0, \tau) = 1$. We constrain this value at τ_{\min} and τ_{\max} for a given acquisition scheme, which produces a close-to-straight line along this boundary between these points. Outside of the constrained points $\hat{E}(\mathbf{q} = 0, \tau)$ will deviate from the boundary condition and eventually also attenuate to zero, limiting the accuracy of $q\tau$ -index estimation when extrapolating beyond τ_{\max} . We do not constrain the second boundary case at $\hat{E}(\mathbf{q}, \tau = 0) = 1$ as it is of no consequence to the estimation of $q\tau$ -indices.

On EAP Positivity: The EAP, being a probability density, should be positive definite. With this in mind, we experimented with adding additional positivity constraints at a range of position in the EAP as was done for the spatial MAP-MRI basis (Özarslan et al., 2013b). However, we found that the number of points that needs to be constrained in four-dimensional $q\tau$ -space causes excessively long computation times, making this approach unfeasible. Fortunately, we find that our Laplacian regularization often produces a positive EAP in practice. The reasoning behind this is that EAP negativity is predominantly caused by oscillatory behavior due to spurious signal extrapolation beyond \mathbf{q}_{\max} . Laplacian regularization imposes signal smoothness also beyond \mathbf{q}_{\max} , resulting in a similarly smooth and very often positive EAP. This result corresponds with previous findings in using Laplacian regularization for MAP-MRI (Fick et al., 2016c).

5.3. Future Applications of $q\tau$ -dMRI

In this last section, we discuss some possible applications of $q\tau$ -dMRI and how it may be used to explore tissue microstructure.

Time-dependent orientation distribution functions: Orientation distribution functions (ODFs) have long been a tool for dMRI techniques to estimate the angular features of the diffusion process (Tristán-Vega et al., 2009; Aganj et al., 2010). However, a recent study suggests that current diffusion-based tractography algorithms based on only the angular features of diffusion are fundamentally ill-posed; consistently finding false-positive connections (Maier-Hein et al., 2016). The authors of this study point out that integrating diffusion microstructure models inside tractography algorithms, i.e., microstructure-informed tractography (Girard et al., 2015; Daducci et al., 2016), may be a viable solution in overcoming this challenge. While we did not explore it in this work, $q\tau$ -dMRI allows for the estimation of *time-dependent* ODFs. In quantifying time-dependent features of different axon bundles, $q\tau$ -dMRI has the potential of providing such microstructure-informed tractography algorithms with time-dependent features. These features could aid in discriminating axon bundles, either from the approach itself or as a preprocessing for other methods as in Fick et al. (2016c).

7D sparse diffusion MRI: To reduce the number of required samples we impose sparsity in the coefficients of $q\tau$ -dMRI, which describe the four-dimensional $q\tau$ -space. In other works, compressed sensing approaches have been used to reduce the number of required samples in the combined six-dimensional kq -space (Sun et al., 2015; Cheng et al., 2015a; Mani et al., 2015). In particular, Cheng et al. (2015a) first use dictionary learning with the SPFI functional basis to learn atoms of 3D q -space, to then do the 6D compressed sensing reconstruction in kq -space. Replacing the SPFI basis with our $q\tau$ -dMRI basis we could extend this approach towards 7D $kq\tau$ -space compressed sensing.

Acquisition design in $q\tau$ -dMRI: Fully sampling the four-dimensional $q\tau$ -space requires many measurements and is an energy- and time-consuming process. In this work, we used methods for optimal q -space acquisition design (Caruyer et al., 2013) to find a scheme for one diffusion time and then copied it for each measured diffusion time. To further optimize $q\tau$ -dMRI acquisition schemes over diffusion time, we could potentially use a Monte-Carlo incoherent sampling approach along the lines of Lustig et al. (2007). In their approach, they suggest to take samples according to a probability density function. However, to apply this method to $q\tau$ -acquisition design, we need to define an appropriate sampling density over the combined 3D q -space and diffusion time space, which is not straightforward.

6. Conclusion

We proposed a novel functional basis approach, that we call $q\tau$ -diffusion MRI ($q\tau$ -dMRI), to simultaneously represent the diffusion signal and Ensemble Average Propagator (EAP) over both three-dimensional q -space and diffusion time τ . To the best of our knowledge, our approach is the first to represent this $q\tau$ -space using a non-parametric approach. Using effective regularization, imposing both signal smoothness and sparsity, we are able to accurately fit $q\tau$ -dMRI using as little as 200 DWIs using 150 basis coefficients.

Once $q\tau$ -dMRI is fitted, we can interpolate any diffusion time from the reconstructed $q\tau$ -EAP and estimate any previously proposed q -space indices. We refer to these time-dependent q -space indices as $q\tau$ -indices. Using $q\tau$ -dMRI to estimate *directional* $q\tau$ -indices like the Return-To-Axis and Plane Probability (RTAP and RTPP), we can probe these properties *directionally*, allowing us to study parallel and perpendicular diffusion separately.

In an *in-vivo* test-retest study of two C57B16 wild-type mice, we also find good reproducibility of estimated of $q\tau$ -indices. We find close-to-Gaussian diffusion parallel and restricted diffusion

perpendicular to the estimated axon axis, corresponding to what we expect in anisotropic white matter. $q\tau$ -dMRI is the first of its kind in being specifically designed to provide open interpretation of the $q\tau$ -diffusion signal in the hopes of opening up new τ -dependent venues of studying nervous tissues.

Acknowledgments

This work was partly supported by ANR “MOSIFAH” under ANR-13-MONU-0009-01, the ERC under the European Union’s Horizon 2020 research and innovation program (ERC Advanced Grant agreement No 694665:CoBCoM), MAXIMS grant funded by ICM’s The Big Brain Theory Program and ANR-10-IAIHU-06.

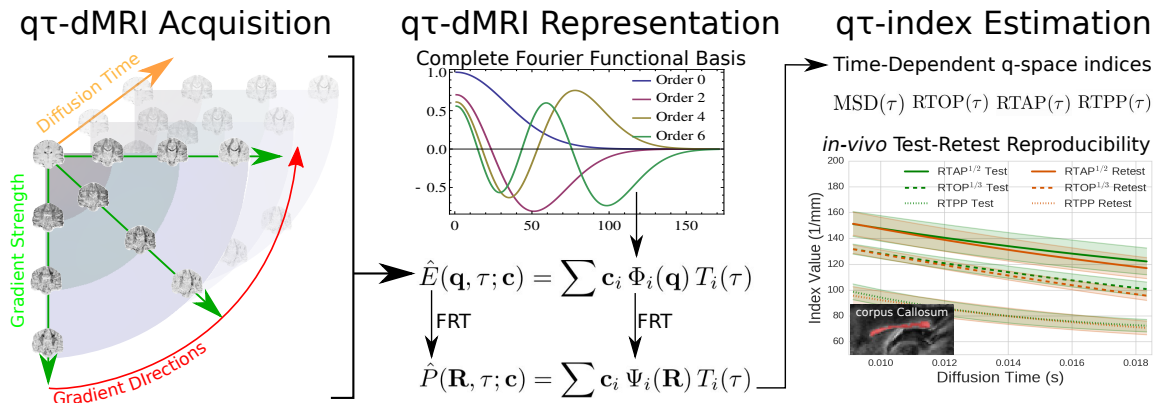


Figure 1: Graphical Abstract. On the left we show a schematic representation of a four-dimensional $q\tau$ -acquisition, varying over gradient strength, directions and diffusion time. Our $q\tau$ -dMRI approach represents the $q\tau$ -diffusion signal using a functional *Fourier* basis. This allows for the analytic reconstruction of the *time dependent* Ensemble Average Propagator (EAP). From the EAP, we can then estimate *time-dependent* q-space indices, that we call $q\tau$ -indices. We do an *in-vivo* test-retest study in the corpus callosum of two mice, showing good reproducibility of estimated $q\tau$ -indices.

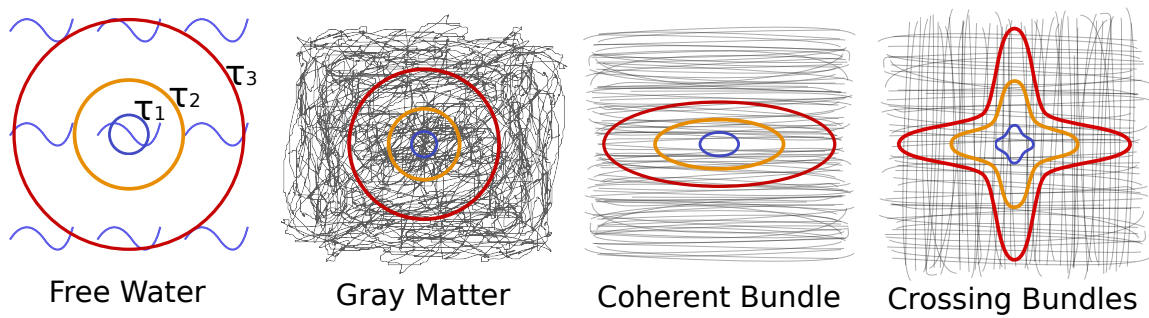


Figure 2: Schematic representations of different tissue types with their corresponding $P(\mathbf{R}, \tau)$ isocontours for different diffusion times $\tau_1 < \tau_2 < \tau_3$. Longer τ increases the likelihood that particles travel further, indicated by the smaller blue isocontour for τ_1 to the largest red isocontour for τ_3 . The shape of the isocontour depends on the structure of the surrounding tissue. Diffusion is considered free in free water, hindered in gray matter and restricted in white matter bundles. Image inspired by [Alexander \(2006\)](#).

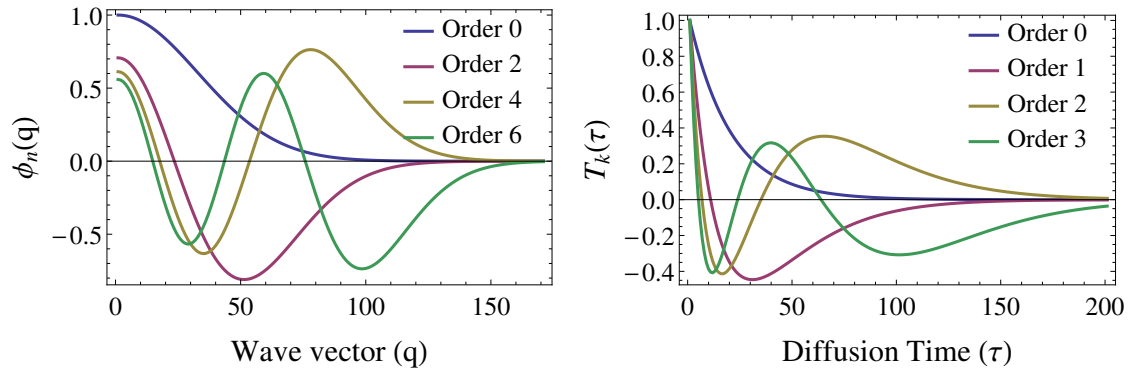


Figure 3: Illustration of the spatial basis functions (left) and temporal basis functions (right). In both cases only the zeroth basis function don't oscillate, when the $\phi_0(q)$ is purely Gaussian and $T_0(\tau)$ is a pure negative exponential. Higher order basis functions oscillate faster and faster. Truncating the basis at a particular order therefore puts a limit on the maximum frequency that can be captured by the basis.

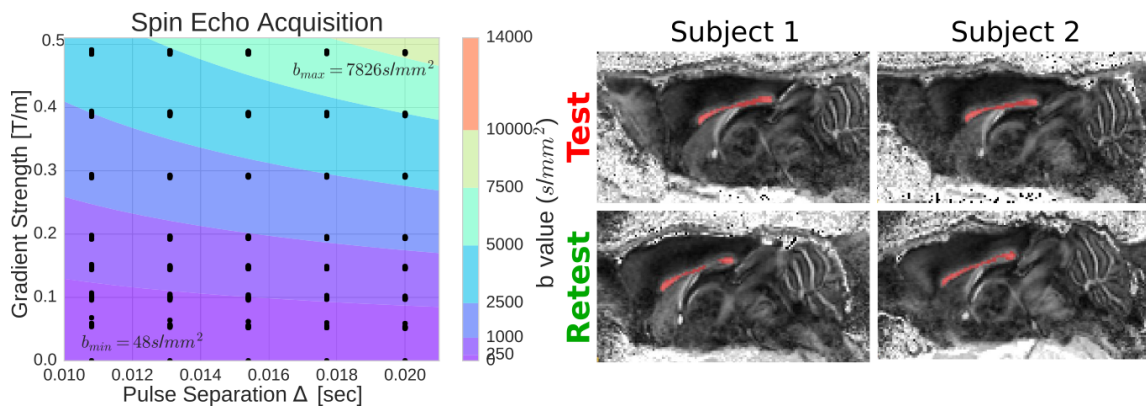


Figure 4: left: the 35 shell $q\tau$ -diffusion acquisition using a spin echo sequence. Every group of point represents a shell with uniformly spread DWIs on the sphere and one b_0 image. The contours represent b-value isolines, given as $b = G^2\delta^2\gamma^2(\Delta - \delta/3)$, whose values are given in the colorbar. The slight spread is due to field inhomogeneities in the *in-vivo* acquisition and are not present in the synthetic simulations. right: FA illustrations of the test-retest mice with in red the region of interest (ROI) voxels in the corpus callosum.

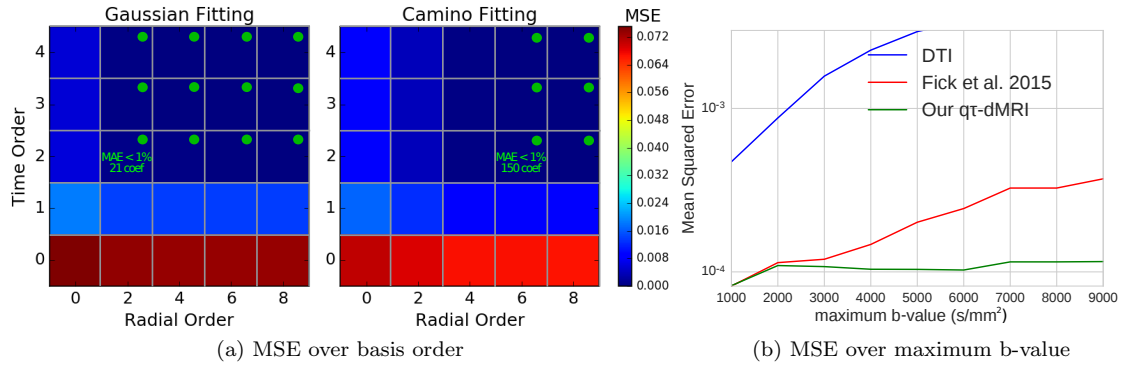


Figure 5: (a) Mean Squared Error (MSE) of noise-free fitting of data generated using an anisotropic Gaussian Tensor (left) and the Camino data from Table 1 (right) using different radial and time orders using our $q\tau$ -dMRI. The color intensity shows the MSE and the green dots indicate orders for which the mean absolute error of the reconstruction is smaller than 1% of the b_0 value. For Gaussian data this is achieved at radial / temporal order 2/2 using 21 coefficients, while for Camino data this is 6/2 using 150 coefficients. (b) Comparison of the fitting error between DTI, the previous approach of Fick et al. (2015a) and our $q\tau$ -dMRI over maximum b-value. Our approach performs better especially when higher b-values are included in the data.

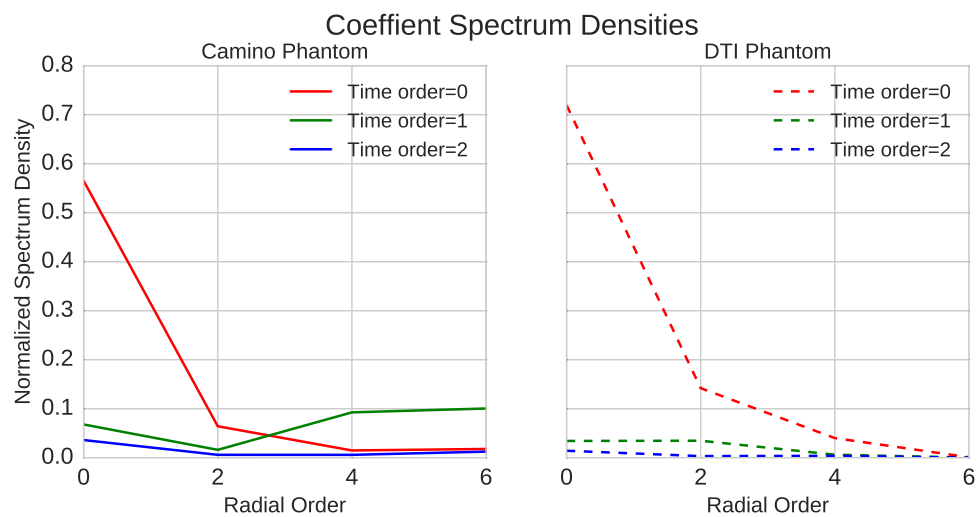


Figure 6: Plot of the normalized spectrum densities of $q\tau$ -dMRI coefficients per radial and temporal order. The coefficient spectra of the Camino (left) and DTI (right) phantom are given in solid and dashed lines, respectively. The time orders zero, one and two are represented as red, green and blue. It can be seen that the spectrum density for both phantoms is most concentrated in radial/temporal order of 0/0, after which the density decreases when either time or radial order is increased. In the Camino phantom there is still some density in the time order=1 coefficients, but the density decreases further for time order=2. For the DTI data there is much less density in the time order=1,2 coefficients compared to the Camino data.

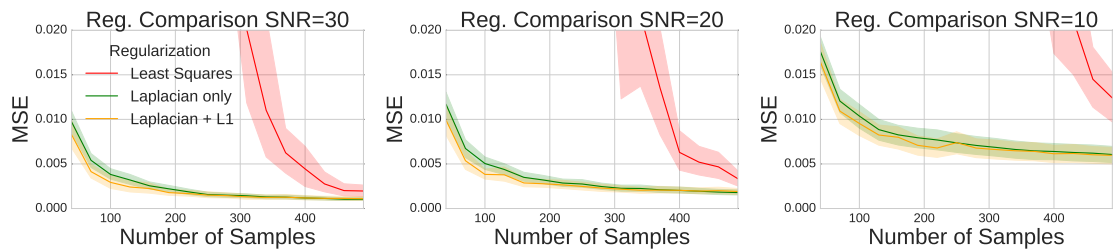


Figure 7: Comparison of fitting error between regularization techniques using random subsampling at $\text{SNR}=\{30,20,10\}$. Overall, the lower the SNR the higher the MSE for every technique. In all cases using only least squares (red) results in by far the highest MSE. Using only Laplacian (green) already stabilizes the MSE much better. Using both Laplacian and ℓ_1 (yellow) produces the lowest result, especially at lower number of samples.

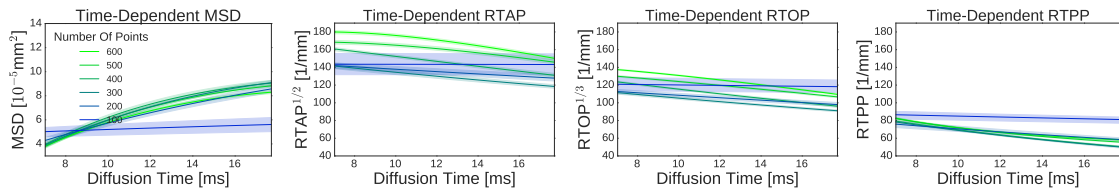


Figure 8: The effect of random subsampling from 600 DWIs (green) to 100 DWIs (blue) on the estimation of q_7 -indices. We show $RTAP^{1/2}$ and $RTOP^{1/3}$ to put them in the same unit as $RTPP$. Notice that $RTAP^{1/2} > RTOP^{1/3} > RTPP$. MSD and $RTPP$ are relatively unaffected by subsampling until they show flat profiles at 100 DWIs. $RTAP$, sensing the perpendicular diffusion direction, decreases as less data is used. $RTOP$, sensing the overall signal, behaves in between $RTAP$ and $RTPP$.

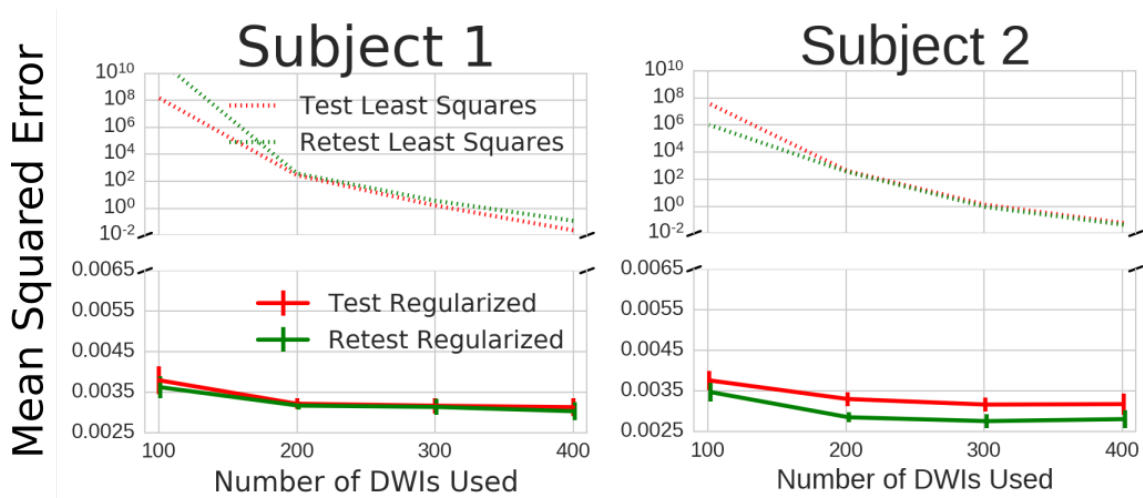


Figure 9: Regularized fitting error of our model while randomly subsampling the data from 400 to 100 fitted DWIs. We broke the y-axis into two parts. The top part uses log-scaling to show the much higher fitting error of unregularized q τ -dMRI. The bottom part uses regular scaling and shows our much lower regularized fitting error. For the regularized result, we see that the fitting error is robust to subsampling for all data sets.

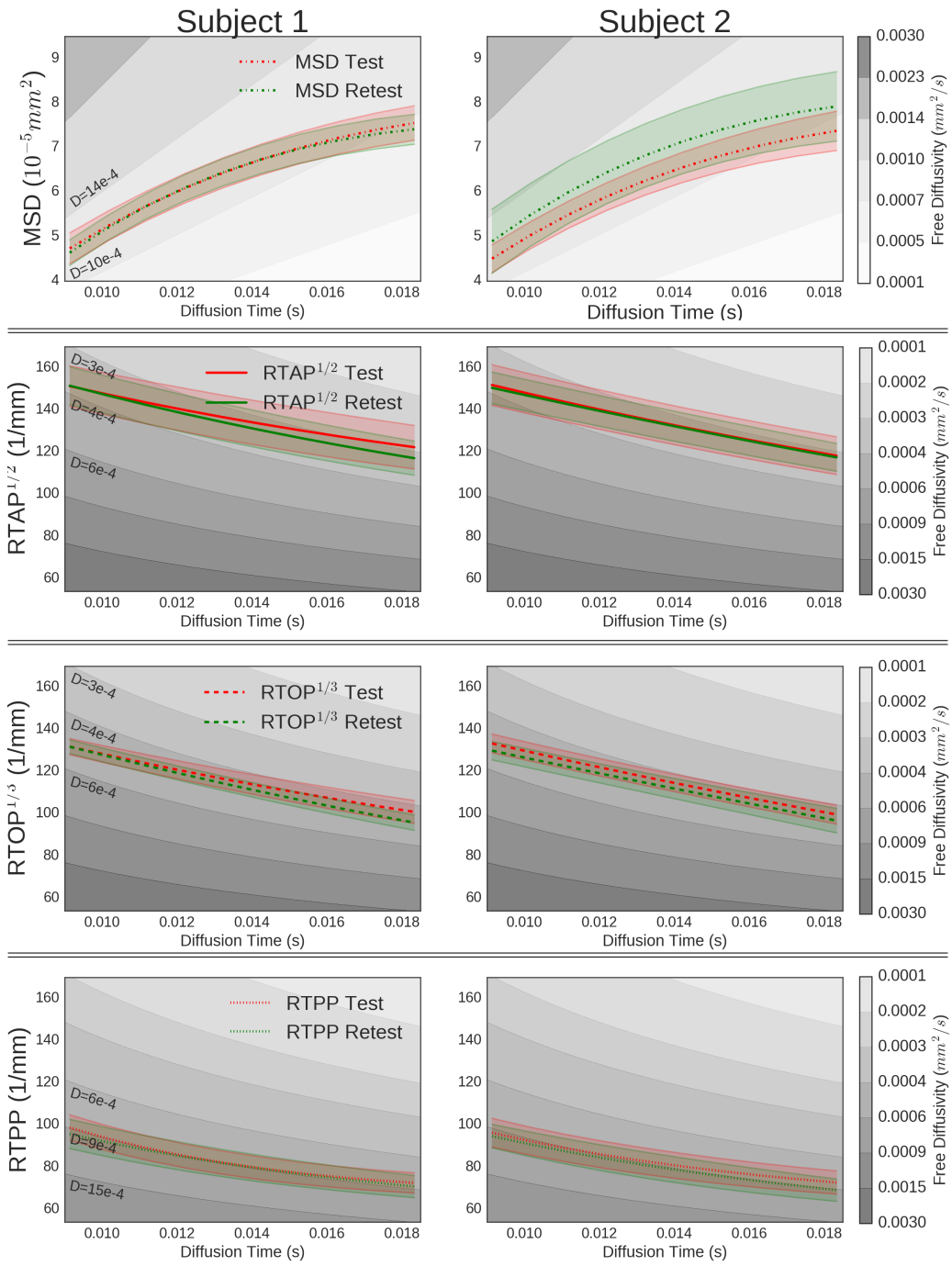


Figure 10: Mean and $0.75 \times$ Standard deviation of the MSD (top) and RTOP, RTAP and RTPP (bottom) in the corpus callosum for the test and retest data (red and green) of both subjects. We used a 0.75 multiplier to better separate index groups. For comparison, the gray tones show MSD isolines for different free diffusion coefficients. In subject 1 the test-retest indices overlap closely for every metric, indicating excellent reproducibility. Subject 2 shows similar overlap for q-space indices, but the MSD is slightly off.

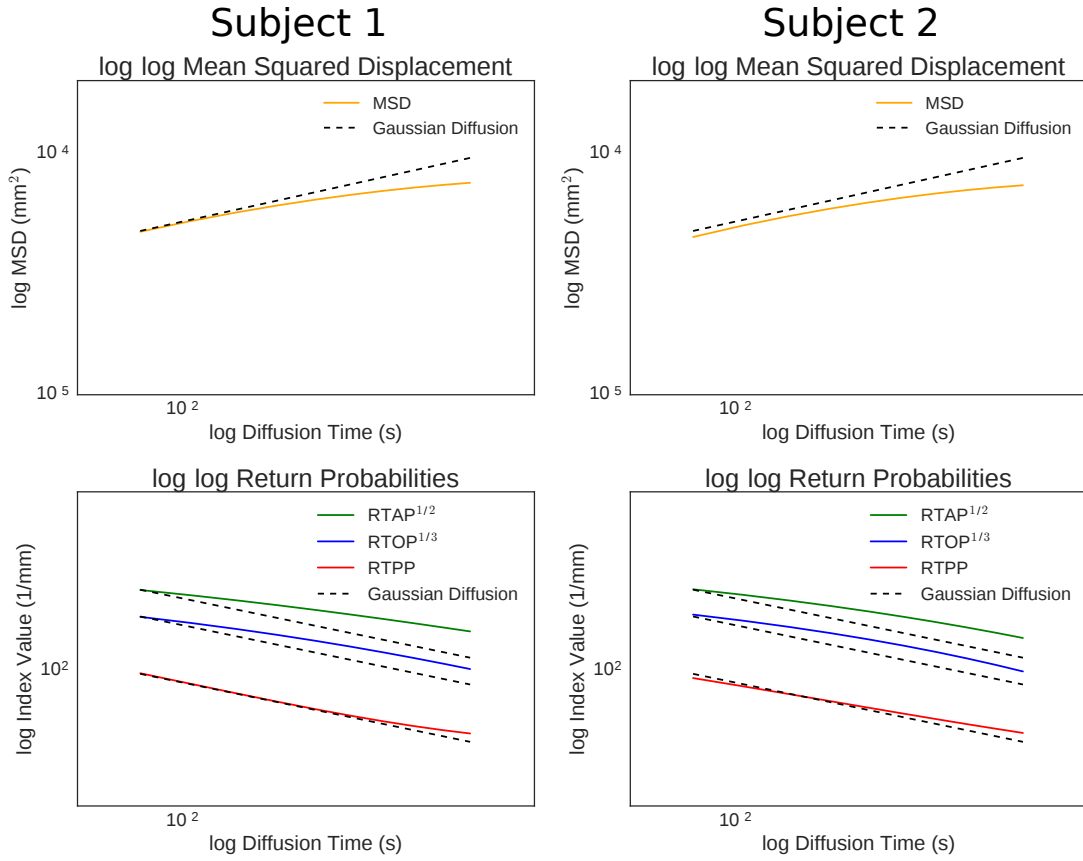


Figure 11: Log-log plots of mean MSD (top) and mean return probabilities (bottom) of both Test Subjects. The dashed lines are the index values for free Gaussian diffusion with diffusivities chosen such that the estimated and Gaussian index values of Subject 1 start at the same place. Power-laws of the form $y = ax^k$ show as straight lines in log-log plots. In Subject 1, notice that the estimated MSD starts close to Gaussian and then slowly diverges at longer τ . Similarly the RTPP, describing parallel diffusion, is almost completely Gaussian over diffusion time. RTAP^{1/2} has a non-Gaussian slope from the start, and RTOP has non-Gaussianity between RTAP^{1/2} and RTPP. The trends between subjects are very similar, but differ slightly in MSD and RTPP.

Table 1: Simulated axon Gamma distributions, sorted by mean axonal diameter $\langle D \rangle$. The left column shows the reference paper for the distribution. The α and β parameters describe the shape and scale of the Gamma distribution with mean diameter $\langle D \rangle = 2\alpha\beta$.

Reference	shape (α)	scale (β) [μm]	$\langle D \rangle$ [μm]
Aboitiz et al. (1992)	3.2734	2.4563e-01	1.60
Aboitiz et al. (1992)	2.8771	2.4932e-01	1.43
Aboitiz et al. (1992)	4.8184	1.3008e-01	1.25
Aboitiz et al. (1992)	3.5027	1.6331e-01	1.14
Aboitiz et al. (1992)	5.3316	1.0242e-01	1.09
Lamantia and Rakic (1990)	5.2051	1.0227e-01	1.06
Lamantia and Rakic (1990)	5.2357	9.3946e-02	0.98
Lamantia and Rakic (1990)	10.1960	3.6983e-02	0.75
Lamantia and Rakic (1990)	8.5358	3.7369e-02	0.64
Lamantia and Rakic (1990)	5.9242	5.3249e-02	0.63
Lamantia and Rakic (1990)	16.2750	1.4282e-02	0.46

Appendix A. q τ -dMRI Implementation

We implemented q τ -dMRI within the Diffusion Imaging In Python (dipy) open-source framework (Garyfallidis et al., 2014). For every voxel, we have the q τ -signal attenuation $y_i = E(\mathbf{q}_i, \tau_i)$, and the corresponding q τ -space positions $\{\mathbf{q}_i, \tau_i\}$, where $i \in [0 \dots, N_s - 1]$ with N_s the number of measured DWIs. Using this input our implementation consists of the following steps:

1. **Scale Factor Estimation:** We first estimate the spatial and temporal scale factors that scale the q τ -dMRI basis to the scale of the data. To estimate the spatial scaling factors we first estimate the 3×3 symmetric displacement matrix \mathbf{A} by only considering only the q-space positions of the data (Basser, 2002). It is estimated using least squares as $\mathbf{A} = \operatorname{argmin}_{\mathbf{A}} \sum_{i=0}^{N_s} \|y_i - \exp(-2\pi^2 \mathbf{q}_i^T \mathbf{A} \mathbf{q}_i)\|^2$. It can be seen as estimating a diffusion tensor in q-space, where we treat the data as if we are ignorant of the diffusion time of any sample. We obtain the spatial scale factors $u_s = \{u_x, u_y, u_z\}$ and rotation matrix \mathbf{R} as the eigenvalues and eigenvectors of \mathbf{A} . It must be ensured that the scale factors are positive. We estimate the temporal scaling factor by directly fitting the first temporal basis function to the data in a similar way as $u_t = \operatorname{argmin}_{u_t} \sum_{i=0}^{N_s} \|y_i - \exp(-\tau_i u_t / 2)\|^2$.
2. **Rotate q-space:** To adhere to the requirements of our spatial MAP-MRI basis, we then rotate q-space points to orthogonalize the data into the Cartesian coordinate system as $\mathbf{q}^* = \mathbf{R} \mathbf{q}$. In this way u_x will describe the spring stiffness of the data along the x-axis, and the same for the other directions.
3. **Diffusion Time Rescaling:** To appropriately weight the spatial and temporal parts of the Laplacian matrix we internally rescale $\tau^* = \tau(u_t / \tilde{u}_s)$ and scale factor $u_t^* = \tilde{u}_s$ with $\tilde{u}_s = (u_x + u_y + u_z) / 3$ the mean spatial scale factor.
4. **Observation and Laplacian Matrix Computation:** Using $\{u_x, u_y, u_z\}$, the rotated \mathbf{q}^* positions, u_t^* , and the scaled τ^* we compute the design matrix $\mathbf{Q}_{ij} = \Xi_j(\mathbf{q}_i, \tau_i, \mathbf{A}, u_t)$, where Ξ is formulated in Eq. (9). We also estimate Laplacian regularization matrix \mathbf{U} as outlined in Section 2.3. The explicit formulation of \mathbf{U} is given Appendix B.
5. **Optimal Regularization Weight Estimation:** To avoid a very time-consuming two-dimensional grid search for optimal Laplacian weighting parameter λ and ℓ_1 weighting parameter α in Eq. (12), we first find optimal λ using generalized cross-validation (GCV) (Craven and Wahba, 1978; Koay et al., 2009) and then use five-fold cross-validation to find optimal α given optimal λ . GCV is based on an N_{data} -fold cross validation. The estimation of λ can be calculated as the minimum argument of the GCV function

$$GCV(\lambda, \mathbf{y}) = \frac{\|\mathbf{y} - \hat{\mathbf{y}}_\lambda\|}{N_{\text{data}} - \operatorname{Tr}(\mathbf{S}_\lambda)} \quad (\text{A.1})$$

where $\mathbf{S}_\lambda = \mathbf{Q}(\mathbf{Q}^T \mathbf{Q} + \lambda \mathbf{U})^{-1} \mathbf{Q}^T$ is the smoother matrix and $\hat{\mathbf{y}}_\lambda = \mathbf{S}_\lambda \mathbf{y}$.

6. **Constraint Matrix Estimation:** We impose the boundary constraint $E(0, \tau) = 1$ only on points $\{\mathbf{q}, \tau\} = \{0, \tau_{\min}\}$ and $\{0, \tau_{\max}\}$ of the measured data. We do this by generating two design matrices \mathbf{Q}_{\min}^τ and \mathbf{Q}_{\max}^τ that map the estimated coefficients \mathbf{c} to the constrained points such that $\tilde{E}(0, \tau_{\min}) = \mathbf{Q}_{\min}^\tau \mathbf{c}$ and $\tilde{E}(0, \tau_{\max}) = \mathbf{Q}_{\max}^\tau \mathbf{c}$.
7. **Coefficient Estimation:** We feed \mathbf{Q} , \mathbf{U} and optimal λ and α and constraint matrices \mathbf{Q}_{\min}^τ and \mathbf{Q}_{\max}^τ into a convex optimization framework CVXPY (Diamond and Boyd, 2016) as in Eq. (12) and estimate the q τ -basis coefficients for the data in this voxel.

8. **Estimation of $q\tau$ -EAP Properties** To estimate $q\tau$ -indices we take advantage of the modular build of our basis. For a given diffusion time τ we first evaluate the temporal part of our basis to produce MAP-MRI coefficients such that $\mathbf{c}_i^{\text{MAP}} = \mathbf{c}_i T_i(\tau, u_t)$. This eliminates the temporal order of our basis so we can heap together the coefficients with the same radial order, leaving us with a standard MAP-MRI representation (Özarslan et al., 2013b). From this representation we can estimate any previously proposed quantity such as q -space indices or ODFs in closed form (Özarslan et al., 2013b; Fick et al., 2016c). Alternatively, $q\tau$ -signal values can be interpolated from the fitted $q\tau$ -dMRI representation by $\mathbf{y}_{\text{interpolated}} = \mathbf{Q}_{\text{interpolation}} \mathbf{c}$ where $\mathbf{Q}_{\text{interpolation}}$ is a new design matrix that maps the coefficients to any point in the $q\tau$ -signal space.

Appendix B. Analytic Laplacian Regularization

We provide the analytic form of the Laplacian regularization matrix in Eq. (11). As our basis is separable in \mathbf{q} and τ , the Laplacian of our basis function Ξ_i is

$$\nabla_{\mathbf{q}\tau}^2 \Xi_i(\mathbf{q}, \tau, u_s, u_t) = (\nabla_{\mathbf{q}}^2 \Phi_i(\mathbf{q}, u_s)) T_i(\tau, u_t) + \Phi_i(\mathbf{q}, u_s) (\nabla_{\tau}^2 T_i(\tau, u_t)) \quad (\text{B.1})$$

with $\nabla_{\mathbf{q}}^2$ and ∇_{τ}^2 the Laplacian to either \mathbf{q} or τ . We then rewrite Eq. (11) as

$$\begin{aligned} \mathbf{U}_{ik} &= \int_{\mathbb{R}} (\nabla_{\mathbf{q}}^2 \Phi_i) (\nabla_{\mathbf{q}}^2 \Phi_k) d\mathbf{q} \int_{\mathbb{R}} T_i T_k d\tau + \int_{\mathbb{R}} \Phi_i \Phi_k d\mathbf{q} \int_{\mathbb{R}} (\nabla_{\tau}^2 T_i) (\nabla_{\tau}^2 T_k) d\tau \\ &\quad + \int_{\mathbb{R}} (\nabla_{\mathbf{q}}^2 \Phi_i) \Phi_k d\mathbf{q} \left(\int_{\mathbb{R}} T_i (\nabla_{\tau}^2 T_k) d\tau + \int_{\mathbb{R}} (\nabla_{\tau}^2 T_i) T_k d\tau \right) \end{aligned} \quad (\text{B.2})$$

Eq. (B.2) can be calculated to a closed form using the orthogonality of physicists' Hermite polynomials with respect to weighting function e^{-x^2} on $[-\infty, \infty]$. Let us first consider the integrals with respect to \mathbf{q} , which are parts of the Laplacian regularization functional of the MAP basis (Fick et al., 2016c). Writing the second order derivative as a double apostrophe "", the Laplacian of the spatial basis is given in terms of the 1D-SHORE functions as $\nabla_{\mathbf{q}}^2 \Phi_i = \phi''_{n_x} \phi_{n_y} \phi_{n_z} + \phi_{n_x} \phi''_{n_y} \phi_{n_z} + \phi_{n_x} \phi_{n_y} \phi''_{n_z}$. The integral of the product of two Laplacians therefore becomes a sum of 9 terms, but can be described using the following three equations:

$$\begin{aligned} \mathbf{U}_n^m(u) &= \int_{\mathbb{R}} \phi''_n \phi''_m d\mathbf{q} = u^3 2(-1)^n \pi^{7/2} \left(\delta_n^m 3(2n^2 + 2n + 1) + \delta_n^{m+4} \sqrt{n!/m!} \right. \\ &\quad \left. + \delta_{n+2}^m (6 + 4n) \sqrt{m!/n!} + \delta_{n+4}^m \sqrt{m!/n!} + \delta_n^{m+2} (6 + 4m) \sqrt{n!/m!} \right) \\ \mathbf{V}_n^m(u) &= \int_{\mathbb{R}} \phi''_n \phi_m d\mathbf{q} = u(-1)^{n+1} \pi^{3/2} \left(\delta_n^m (1 + 2n) + \delta_n^{m+2} \sqrt{n(n-1)} + \delta_{n+2}^m \sqrt{m(m-1)} \right) \\ \mathbf{W}_n^m(u) &= \int_{\mathbb{R}} \phi_n \phi_m d\mathbf{q} = u^{-1} \delta_n^m (-1)^n / (2\pi^{1/2}) \end{aligned} \quad (\text{B.3})$$

Using the functions in Eq. (B.3) we define the \mathbf{q} -dependent parts of Eq. (B.2) as (Fick et al., 2016b):

$$\begin{aligned} \int_{\mathbb{R}} (\nabla_{\mathbf{q}}^2 \Phi_i)(\nabla_{\mathbf{q}}^2 \Phi_k) d\mathbf{q} &= \frac{u_x^3}{u_y u_z} U_{x_i}^{x_k} W_{y_i}^{y_k} W_{z_i}^{z_k} + 2 \frac{u_x u_y}{u_z} V_{x_i}^{x_k} V_{y_i}^{y_k} W_{z_i}^{z_k} + \frac{u_y^3}{u_z u_x} U_{y_i}^{y_k} W_{z_i}^{z_k} W_{x_i}^{x_k} \\ &\quad + 2 \frac{u_y u_z}{u_x} V_{y_i}^{y_k} V_{z_i}^{z_k} W_{x_i}^{x_k} + \frac{u_z^3}{u_x u_y} U_{z_i}^{z_k} W_{x_i}^{x_k} W_{y_i}^{y_k} + 2 \frac{u_x u_z}{u_y} V_{x_i}^{x_k} V_{z_i}^{z_k} W_{y_i}^{y_k} \\ \int_{\mathbb{R}} (\nabla_{\mathbf{q}}^2 \Phi_i)(\Phi_k) d\mathbf{q} &= \frac{u_x}{u_y u_z} V_{x_i}^{x_k} W_{y_i}^{y_k} W_{z_i}^{z_k} + \frac{u_y}{u_x u_z} V_{x_i}^{x_k} W_{y_i}^{y_k} W_{z_i}^{z_k} + \frac{u_z}{u_x u_y} V_{x_i}^{x_k} W_{y_i}^{y_k} W_{z_i}^{z_k} \\ \int_{\mathbb{R}} \Phi_i \Phi_k d\mathbf{q} &= \frac{1}{u_x u_y u_z} W_{x_i}^{x_k} W_{y_i}^{y_k} W_{z_i}^{z_k} \end{aligned}$$

For terms with τ , we denote the operator $M_{x_1}^{x_2} = \min(x_1, x_2)$ for the minimal value of x_1, x_2 and H_x the Heaviside step function with $H_x = 1$ iff $x \geq 0$.

$$\begin{aligned} \int_{\mathbb{R}} (\nabla_{\tau}^2 T_i)(\nabla_{\tau}^2 T_k) d\tau &= \left(\frac{1}{4} |o(i) - o(k)| + \frac{1}{16} \delta_{o(i)}^{o(k)} + M_{o(i)}^{o(k)} \right. \\ &\quad \left. + \sum_{p=1}^{M_{o(i)}^{o(k)}+1} (o(i) - p)(o(k) - p) H_{M_{o(i)}^{o(k)}-p} + H_{o(i)-1} H_{o(k)-1} \left(o(i) + o(k) - 2 \right. \right. \\ &\quad \left. \left. + \sum_{p=0}^{M_{o(i)}^{o(k)}-2} p + \sum_{p=0}^{M_{o(i)}^{o(k)}-2} p + M_{o(i)-1}^{o(k)-1} (|o(i) - o(k)| - 1) H_{(|o(i)-o(k)|-1)} \right) \right) \\ \left(\int_{\mathbb{R}} T_i (\nabla_{\tau}^2 T_k) d\tau + \int_{\mathbb{R}} (\nabla_{\tau}^2 T_i) T_k d\tau \right) &= u_t \left(\frac{1}{2} \delta_{o(i)}^{o(k)} + (1 - \delta_{o(i)}^{o(k)}) \cdot |o(i) - o(k)| \right) \\ \int_{\mathbb{R}} T_i T_k d\tau &= 1/u_t \delta_{o(k)}^{o(i)} \end{aligned}$$

Appendix C. Isotropic Analytic Laplacian Regularization

The isotropic implementation of MAP-MRI (Özarslan et al., 2013b, Appendix A), which is equivalent to 3D-SHORE (Merlet and Deriche, 2013), describes the signal and EAP as

$$\hat{E}(\mathbf{q}, \tau; \mathbf{c}) = \sum_i^{N_{\mathbf{q}}} \sum_k^{N_{\tau}} \mathbf{c}_{ik} \Phi_i^{\text{SHO}}(\mathbf{q}) T_k(\tau) T_k(\tau) \quad (\text{C.1})$$

3D-SHORE's signal and EAP basis functions are given as

$$\Phi_{jlm}^{\text{SHO}}(\mathbf{q}, u_0) = \sqrt{4\pi} i^{-l} (2\pi^2 u_0^2 q^2)^{l/2} e^{-2\pi^2 u_0^2 q^2} L_{j-1}^{l+1/2} (4\pi^2 u_0^2 q^2) Y_l^m(\mathbf{u}) \quad (\text{C.2})$$

$$\Psi_{jlm}^{\text{SHO}}(\mathbf{R}, u_0) = \frac{(-1)^{j-1}}{\sqrt{2\pi} u_0^3} \left(\frac{R^2}{2u_0^2} \right)^{l/2} e^{-R^2/2u_0^2} L_{j-1}^{l+1/2} \left(\frac{R^2}{u_0^2} \right) Y_l^m(\mathbf{r}) \quad (\text{C.3})$$

where $\Phi = \text{IFT}(\Psi)$ and $j = (n + 2 - l)/2$ is related to the radial order n and angular order l of the basis where $j \geq 1, l \geq 0$. The real spherical harmonic basis Y_l^m (Descoteaux et al., 2007) has angular order l and phase factor m such that $-l \leq m \leq l$, and $L_{j-1}^{l+1/2}$ is the generalized Laguerre

polynomial. Following [Özarslan et al. \(2013b\)](#) and formulating the isotropic scaling factor as $U = u_0^2$ and anisotropic scaling factors as $X^2 = u_x^2$, $Y^2 = u_y^2$ and $Z^2 = u_z^2$, we find u_0 as the only positive, real root of the cubic polynomial

$$3XYZ + (XY + XZ + YZ)U - (X + Y + Z)U^2 - 3U^3 = 0. \quad (\text{C.4})$$

Following the same formulation of the $q\tau$ -Laplacian as in Eq. (B.2), the closed-form Laplacian for the isotropic basis is given as ([Fick et al., 2015a](#)):

$$\begin{aligned} \int_{\mathbb{R}} (\nabla_{\mathbf{q}}^2 \Phi_i^{\text{SHO}})(\Phi_k^{\text{SHO}}) d\mathbf{q} &= u_0 \delta_{l(i)}^{l(k)} \delta_{m(i)}^{m(k)} \begin{cases} \delta_{j(i)}^{j(k)+2} \times \frac{2^{2-l} \pi^2 \Gamma(\frac{5}{2} + j(k) + l)}{\Gamma(j(k))} \\ \delta_{j(i)}^{j(k)+1} \times \frac{2^{2-l} \pi^2 (-3 + 4j(i) + 2l) \Gamma(\frac{3}{2} + j(k) + l)}{\Gamma(j(k))} \\ \delta_{j(i)}^{j(k)} \times \frac{2^{-l} \pi^2 (3 + 24j(i)^2 + 4(-2+l)l + 12j(i)(-1+2l)) \Gamma(\frac{1}{2} + j(i) + l)}{\Gamma(j(i))} \\ \delta_{j(i)}^{j(k)-1} \times \frac{2^{2-l} \pi^2 (-3 + 4j(k) + 2l) \Gamma(\frac{3}{2} + j(i) + l)}{\Gamma(j(i))} \\ \delta_{j(i)}^{j(k)-2} \times \frac{2^{2-l} \pi^2 \Gamma(\frac{5}{2} + j(i) + l)}{\Gamma(j(i))} \end{cases} \\ \int_{\mathbb{R}} (\nabla_{\mathbf{q}}^2 \Phi_i^{\text{SHO}})(\Phi_k^{\text{SHO}}) d\mathbf{q} &= \frac{1}{u_s} \delta_{l(i)}^{l(k)} \delta_{m(i)}^{m(k)} \begin{cases} \delta_{(j(i), j(k)+1)} \frac{-2^{-l} \Gamma(\frac{3}{2} + j(k) + l)}{\Gamma(j(k))} \\ \delta_{(j(i), j(k))} \frac{2^{-(l+1)} (1 - 4j(i) - 2l) \Gamma(\frac{1}{2} + j(i) + l)}{\Gamma(j(i))} \\ \delta_{(j(i), j(k)-1)} \frac{-2^{-l} \Gamma(\frac{3}{2} + j(i) + l)}{\Gamma(j(i))} \end{cases} \\ \int_{\mathbb{R}} \Phi_i^{\text{SHO}} \Phi_k^{\text{SHO}} d\mathbf{q} &= \frac{1}{u_s^3} \delta_{j(i)}^{j(k)} \delta_{l(i)}^{l(k)} \delta_{m(i)}^{m(k)} \frac{2^{-(l+2)} \Gamma(j(i) + l + 1/2)}{\pi^2 \Gamma(j)} \end{aligned}$$

Appendix D. Laplacian Regularization Using Basis Normalization

While it was not necessary in practice to normalize our basis when imposing sparsity, we did derive the necessary adaptation to the Laplacian regularizer when the basis is normalized. This is essential when using the isotropic MAP-MRI implementation. To normalize the basis, we first derive the inner product C of each part of the basis:

$$\frac{1}{C^{\text{MAP}}} = \int_{\mathbb{R}^3} \Phi_{N_i}(\mathbf{q}, u_s) \Phi_{N_i}(\mathbf{q}, u_s) d\mathbf{q} = \frac{1}{8u_x u_y u_z \pi^{2/3}} \quad (\text{D.1})$$

$$\frac{1}{C_{jl}^{\text{SHO}}} = \int_{\mathbb{R}^3} \Phi_i^{\text{SHO}}(\mathbf{q}, u_0) \Phi_i^{\text{SHO}}(\mathbf{q}, u_0) d\mathbf{q} = \frac{1}{2^{2+l} \pi^2 u_0^3} \frac{\Gamma(l + j + 1/2)}{(j-1)!} \quad (\text{D.2})$$

$$\frac{1}{C^\tau} = \int_{\mathbb{R}^3} T_i(\tau, u_t) T_i(\tau, u_t) d\tau = \frac{1}{u_t} \quad (\text{D.3})$$

where only the isotropic MAP implementation has a basis order-dependent inner product. A normalized four-dimensional basis function Ξ_i^* is obtained by multiplying the original function Ξ_i as $\Xi_i^* = \sqrt{C_i} \Xi_i$ with

$$\sqrt{C^{\text{MAP}}} = \sqrt{8u_x u_y u_z \pi^{3/4}}, \quad \sqrt{C_{jl}^{\text{SHO}}} = \sqrt{\frac{2^{2+l} \pi^2 u_0^3 (j-1)!}{\Gamma(j+l+1/2)}}, \quad \sqrt{C^\tau} = \sqrt{u_t} \quad (\text{D.4})$$

where the normalization $\sqrt{C_i} = \sqrt{C^{\text{MAP}}C^\tau}$ or $\sqrt{C_i} = \sqrt{C_i^{\text{SHO}}C^\tau}$ depending on the choice of spatial basis. Following Eq. (11) and omitting the scale factor dependence for brevity, every position in the normalized regularization matrix \mathbf{U}^* is given as

$$\mathbf{U}_{ik}^* = \iint \nabla^2 \Xi_i^*(\mathbf{q}, \tau) \cdot \nabla^2 \Xi_k^*(\mathbf{q}, \tau) d\mathbf{q} d\tau \quad (\text{D.5})$$

$$= \sqrt{C_i C_k} \iint \nabla^2 \Xi_i(\mathbf{q}, \tau) \cdot \nabla^2 \Xi_k(\mathbf{q}, \tau) d\mathbf{q} d\tau \quad (\text{D.6})$$

$$= \mathbf{C}_{ik} \mathbf{U}_{ik} \quad (\text{D.7})$$

where it becomes clear that normalized regularization matrix \mathbf{U}^* can be easily computed as the entry-wise product of the original matrix \mathbf{U} in Eq. (B.2) and normalization matrix \mathbf{C} with elements $\mathbf{C}_{ik} = \sqrt{C_i C_k}$.

References

- Aboitiz, F., Scheibel, A.B., Fisher, R.S., Zaidel, E., 1992. Fiber composition of the human corpus callosum. *Brain research* 598, 143–153.
- Aganj, I., Lenglet, C., Sapiro, G., Yacoub, E., Ugurbil, K., Harel, N., 2010. Reconstruction of the orientation distribution function in single-and multiple-shell q-ball imaging within constant solid angle. *Magnetic Resonance in Medicine* 64, 554–566.
- Alexander, D.C., 2006. An introduction to computational diffusion mri: the diffusion tensor and beyond, in: *Visualization and processing of tensor fields*. Springer, pp. 83–106.
- Alexander, D.C., Hubbard, P.L., Hall, M.G., Moore, E.A., Ptito, M., Parker, G.J., Dyrby, T.B., 2010. Orientationally invariant indices of axon diameter and density from diffusion mri. *Neuroimage* 52, 1374–1389.
- Andersson, J.L., Sotiropoulos, S.N., 2016. An integrated approach to correction for off-resonance effects and subject movement in diffusion mr imaging. *Neuroimage* 125, 1063–1078.
- Assaf, Y., Blumenfeld-Katzir, T., Yovel, Y., Basser, P.J., 2008. Axc caliber: a method for measuring axon diameter distribution from diffusion mri. *Magnetic Resonance in Medicine* 59, 1347–1354.
- Assaf, Y., Cohen, Y., et al., 1998. In vivo and in vitro bi-exponential diffusion of n-acetyl aspartate(naa) in rat brain: a potential structural probe? *NMR in biomedicine* 11, 67–74.
- Assaf, Y., Freidlin, R.Z., Rohde, G.K., Basser, P.J., 2004. New modeling and experimental framework to characterize hindered and restricted water diffusion in brain white matter. *Magnetic Resonance in Medicine* 52, 965–978.
- Assemblal, H.E., Tschumperlé, D., Brun, L., 2009. Efficient and robust computation of pdf features from diffusion mr signal. *Medical image analysis* 13, 715–729.
- Avram, A.V., Sarlls, J.E., Barnett, A.S., Özarslan, E., Thomas, C., Irfanoglu, M.O., Hutchinson, E., Pierpaoli, C., Basser, P.J., 2015. Clinical feasibility of using mean apparent propagator (map) mri to characterize brain tissue microstructure. *NeuroImage* .

- Bar-Shir, A., Avram, L., Özarslan, E., Basser, P.J., Cohen, Y., 2008. The effect of the diffusion time and pulse gradient duration ratio on the diffraction pattern and the structural information estimated from q-space diffusion mr: experiments and simulations. *Journal of Magnetic Resonance* 194, 230–236.
- Basser, P.J., 2002. Relationships between diffusion tensor and q-space mri. *Magnetic resonance in medicine* 47, 392–397.
- Basser, P.J., Mattiello, J., LeBihan, D., 1994. Mr diffusion tensor spectroscopy and imaging. *Biophysical journal* 66, 259.
- Beaulieu, C., 2002. The basis of anisotropic water diffusion in the nervous system—a technical review. *NMR in Biomedicine* 15, 435–455.
- Burcaw, L.M., Fieremans, E., Novikov, D.S., 2015. Mesoscopic structure of neuronal tracts from time-dependent diffusion. *NeuroImage* 114, 18–37.
- Callaghan, P.T., 1991. Principles of nuclear magnetic resonance microscopy. volume 3. Clarendon Press Oxford.
- Callaghan, P.T., 1995. Pulsed-gradient spin-echo nmr for planar, cylindrical, and spherical pores under conditions of wall relaxation. *Journal of magnetic resonance, Series A* 113, 53–59.
- Candès, E.J., Romberg, J., Tao, T., 2006. Robust uncertainty principles: Exact signal reconstruction from highly incomplete frequency information. *IEEE Transactions on information theory* 52, 489–509.
- Caruyer, E., Deriche, R., 2012. Diffusion mri signal reconstruction with continuity constraint and optimal regularization. *Medical Image Analysis* 16, 1113–1120.
- Caruyer, E., Lenglet, C., Sapiro, G., Deriche, R., 2013. Design of multishell sampling schemes with uniform coverage in diffusion mri. *Magnetic Resonance in Medicine* 69, 1534–1540.
- Cheng, J., 2014. Estimation and Processing of Ensemble Average Propagator and Its Features in Diffusion MRI. Ph.D. thesis. INRIA Sophia Antipolis - ATHENA.
- Cheng, J., Shen, D., Basser, P.J., Yap, P.T., 2015a. Joint 6d kq space compressed sensing for accelerated high angular resolution diffusion mri, in: *International Conference on Information Processing in Medical Imaging*, Springer. pp. 782–793.
- Cheng, J., Shen, D., Yap, P.T., Basser, P.J., 2015b. Tensorial spherical polar fourier diffusion mri with optimal dictionary learning, in: *International Conference on Medical Image Computing and Computer-Assisted Intervention*, Springer. pp. 174–182.
- Cohen, Y., Assaf, Y., 2002. High b-value q-space analyzed diffusion-weighted mrs and mri in neuronal tissues—a technical review. *NMR in Biomedicine* 15, 516–542.
- Cook, P., Bai, Y., Nedjati-Gilani, S., Seunarine, K., Hall, M., Parker, G., Alexander, D., 2006. Camino: open-source diffusion-mri reconstruction and processing, in: *14th scientific meeting of the international society for magnetic resonance in medicine*, Seattle WA, USA.

- Craven, P., Wahba, G., 1978. Smoothing noisy data with spline functions. *Numerische Mathematik* 31, 377–403.
- Daducci, A., Dal Palú, A., Descoteaux, M., Thiran, J.P., 2016. Microstructure informed tractography: pitfalls and open challenges. *Frontiers in Neuroscience* 10, 247.
- De Santis, S., Jones, D.K., Roebroeck, A., 2016. Including diffusion time dependence in the extra-axonal space improves in vivo estimates of axonal diameter and density in human white matter. *NeuroImage* 130, 91–103.
- Descoteaux, M., Angelino, E., Fitzgibbons, S., Deriche, R., 2007. Regularized, fast, and robust analytical q-ball imaging. *Magnetic Resonance in Medicine* 58, 497–510.
- Descoteaux, M., Deriche, R., Le Bihan, D., Mangin, J.F., Poupon, C., 2011. Multiple q-shell diffusion propagator imaging. *Medical image analysis* 15, 603–621.
- Diamond, S., Boyd, S., 2016. CVXPY: A Python-embedded modeling language for convex optimization. *Journal of Machine Learning Research* To appear.
- Einstein, A., 1956. *Investigations on the Theory of the Brownian Movement*. Courier Corporation.
- Ferizi, U., Scherrer, B., Schneider, T., Alipoor, M., Eufracio, O., Fick, R.H., Deriche, R., Nilsson, M., Loya-Olivas, A.K., Rivera, M., et al., 2016. Diffusion mri microstructure models with in vivo human brain connectom data: results from a multi-group comparison. *arXiv preprint arXiv:1604.07287*.
- Fick, Rutger, H., Pizzolato, M., Wassermann, D., Zucchelli, M., Menegaz, G., Deriche, R., 2016a. A Sensitivity Analysis of Q-space Indices With Respect to Changes in Axonal Diameter, Dispersion and Tissue Composition, in: *International Symposium on BIOMEDICAL IMAGING: From Nano to Macro*, Prague, Czech Republic.
- Fick, R., Petiet, A., Santin, M., Philippe, A.C., Lehericy, S., Deriche, R., Wassermann, D., 2016b. Multi-spherical diffusion mri: Exploring diffusion time using signal sparsity, in: *MICCAI 2016 Workshop on Computational Diffusion MRI (CDMRI'16)*.
- Fick, R., Wassermann, D., Pizzolato, M., Deriche, R., 2015a. A unifying framework for spatial and temporal diffusion in diffusion mri, in: *International Conference on Information Processing in Medical Imaging*, Springer. pp. 167–178.
- Fick, R.H., Wassermann, D., Caruyer, E., Deriche, R., 2016c. Mapl: Tissue microstructure estimation using laplacian-regularized map-mri and its application to hcp data. *NeuroImage* 134, 365–385.
- Fick, R.H., Wassermann, D., Sanguinetti, G., Deriche, R., 2015b. Laplacian-regularized map-mri: Improving axonal caliber estimation, in: *IEEE International Symposium on Biomedical Imaging*, New York City, New York.
- Fieremans, E., Burcaw, L.M., Lee, H.H., Lemberskiy, G., Veraart, J., Novikov, D.S., 2016. In vivo observation and biophysical interpretation of time-dependent diffusion in human white matter. *NeuroImage* 129, 414–427.

- Fieremans, E., Novikov, D.S., Jensen, J.H., Helpert, J.A., 2010. Monte carlo study of a two-compartment exchange model of diffusion. *NMR in Biomedicine* 23, 711–724.
- Garyfallidis, E., Brett, M., Amirbekian, B., Rokem, A., Van Der Walt, S., Descoteaux, M., Nimmo-Smith, I., Contributors, D., 2014. Dipy, a library for the analysis of diffusion mri data. *Frontiers in neuroinformatics* 8.
- Girard, G., Fick, R., Descoteaux, M., Deriche, R., Wassermann, D., 2015. Atract: microstructure-driven tractography based on the ensemble average propagator, in: *International Conference on Information Processing in Medical Imaging*, Springer. pp. 675–686.
- Grosenick, L., Klingenberg, B., Katovich, K., Knutson, B., Taylor, J.E., 2013. Interpretable whole-brain prediction analysis with graphnet. *NeuroImage* 72, 304–321.
- Hosseinbor, A.P., Chung, M.K., Wu, Y.C., Alexander, A.L., 2013. Bessel fourier orientation reconstruction (bfor): An analytical diffusion propagator reconstruction for hybrid diffusion imaging and computation of q-space indices. *NeuroImage* 64, 650–670.
- Hosseinbor, A.P., Chung, M.K., Wu, Y.C., Bendlin, B.B., Alexander, A.L., 2015. A 4d hyperspherical interpretation of q-space. *Medical image analysis* 21, 15–28.
- Hürlimann, M.D., Schwartz, L.M., Sen, P.N., 1995. Probability of return to the origin at short times: A probe of microstructure in porous media. *Physical Review B* 51, 14936.
- Jones, D.K., 2010. *Diffusion mri*. Oxford University Press.
- Kärger, J., Heink, W., 1983. The propagator representation of molecular transport in microporous crystallites. *Journal of Magnetic Resonance (1969)* 51, 1–7.
- Koay, C.G., Özarslan, E., Basser, P.J., 2009. A signal transformational framework for breaking the noise floor and its applications in mri. *Journal of Magnetic Resonance* 197, 108–119.
- Lamantia, A.S., Rakic, P., 1990. Cytological and quantitative characteristics of four cerebral commissures in the rhesus monkey. *Journal of Comparative Neurology* 291, 520–537.
- Lätt, J., Nilsson, M., van Westen, D., Wirestam, R., Ståhlberg, F., Brockstedt, S., 2009. Diffusion-weighted mri measurements on stroke patients reveal water-exchange mechanisms in sub-acute ischaemic lesions. *NMR in biomedicine* 22, 619–628.
- Le Bihan, D., 1995. Molecular diffusion, tissue microdynamics and microstructure. *NMR in Biomedicine* 8, 375–386.
- Le Bihan, D., Breton, E., Lallemand, D., Grenier, P., Cabanis, E., Laval-Jeantet, M., 1986. Mr imaging of intravoxel incoherent motions: application to diffusion and perfusion in neurologic disorders. *Radiology* 161, 401–407.
- Le Bihan, D., Turner, R., Douek, P., 1993. Is water diffusion restricted in human brain white matter? an echo-planar nmr imaging study. *Neuroreport* 4, 887–890.
- Leergaard, T.B., White, N.S., De Crespigny, A., Bolstad, I., D’Arceuil, H., Bjaalie, J.G., Dale, A.M., 2010. Quantitative histological validation of diffusion mri fiber orientation distributions in the rat brain .

- Lustig, M., Donoho, D., Pauly, J.M., 2007. Sparse mri: The application of compressed sensing for rapid mr imaging. *Magnetic resonance in medicine* 58, 1182–1195.
- Maier-Hein, K., Neher, P., Houde, J.C., Cote, M.A., Garyfallidis, E., Zhong, J., Chamberland, M., Yeh, F.C., Lin, Y.C., Ji, Q., et al., 2016. Tractography-based connectomes are dominated by false-positive connections. *bioRxiv* , 084137.
- Mani, M., Jacob, M., Guidon, A., Magnotta, V., Zhong, J., 2015. Acceleration of high angular and spatial resolution diffusion imaging using compressed sensing with multichannel spiral data. *Magnetic resonance in medicine* 73, 126–138.
- Manjón, J.V., Coupé, P., Concha, L., Buades, A., Collins, D.L., Robles, M., 2013. Diffusion weighted image denoising using overcomplete local pca. *PloS one* 8, e73021.
- Merlet, S.L., Deriche, R., 2013. Continuous diffusion signal, eap and odf estimation via compressive sensing in diffusion mri. *Medical image analysis* 17, 556–572.
- Michailovich, O.V., Rathi, Y., 2008. On approximation of orientation distributions by means of spherical ridgelets, in: 2008 5th IEEE International Symposium on Biomedical Imaging: From Nano to Macro, IEEE. pp. 939–942.
- Milford, D., Rosbach, N., Bendszus, M., Heiland, S., 2015. Mono-exponential fitting in t2-relaxometry: Relevance of offset and first echo. *PloS one* 10, e0145255.
- Mitra, P.P., Latour, L., Kleinberg, R.L., Sotak, C.H., 1995. Pulsed-field-gradient nmr measurements of restricted diffusion and the return-to-the-origin probability. *Journal of Magnetic Resonance, Series A* 114, 47–58.
- Moonen, C.T., Pekar, J., de Vleeschouwer, M.H., van Gelderen, P., van Zijl, P., Despres, D., 1991. Restricted and anisotropic displacement of water in healthy cat brain and in stroke studied by nmr diffusion imaging. *Magnetic resonance in medicine* 19, 327–332.
- Ning, L., Laun, F., Gur, Y., DiBella, E.V., Deslauriers-Gauthier, S., Megherbi, T., Ghosh, A., Zucchelli, M., Menegaz, G., Fick, R., et al., 2015. Sparse reconstruction challenge for diffusion mri: Validation on a physical phantom to determine which acquisition scheme and analysis method to use? *Medical image analysis* 26, 316–331.
- Ning, L., Setsompop, K., Westin, C.F., Rathi, Y., 2016. New insights about time-varying diffusivity and its estimation from diffusion mri. *Magnetic Resonance in Medicine* .
- Novikov, D.S., Jensen, J.H., Helpert, J.A., Fieremans, E., 2014. Revealing mesoscopic structural universality with diffusion. *Proceedings of the National Academy of Sciences* 111, 5088–5093.
- Novikov, D.S., Jespersen, S.N., Kiselev, V.G., Fieremans, E., 2016. Quantifying brain microstructure with diffusion mri: Theory and parameter estimation. *arXiv preprint arXiv:1612.02059* .
- Novikov, D.S., Kiselev, V.G., 2010. Effective medium theory of a diffusion-weighted signal. *NMR in Biomedicine* 23, 682–697.

- Özarslan, E., Basser, P.J., Shepherd, T.M., Thelwall, P.E., Vemuri, B.C., Blackband, S.J., 2006. Observation of anomalous diffusion in excised tissue by characterizing the diffusion-time dependence of the mr signal. *Journal of Magnetic Resonance* 183, 315–323.
- Özarslan, E., Koay, C.G., Basser, P.J., 2013a. Simple harmonic oscillator based reconstruction and estimation for one-dimensional q-space magnetic resonance (1d-shore), in: *Excursions in Harmonic Analysis, Volume 2*. Springer, pp. 373–399.
- Özarslan, E., Koay, C.G., Shepherd, T.M., Komlosh, M.E., İrfanoğlu, M.O., Pierpaoli, C., Basser, P.J., 2013b. Mean apparent propagator (map) mri: a novel diffusion imaging method for mapping tissue microstructure. *NeuroImage* 78, 16–32.
- Özarslan, E., Shemesh, N., Koay, C.G., Cohen, Y., Basser, P.J., 2011. Nuclear magnetic resonance characterization of general compartment size distributions. *New journal of physics* 13, 015010.
- Özarslan, E., Shepherd, T.M., Koay, C.G., Blackband, S.J., Basser, P.J., 2012. Temporal scaling characteristics of diffusion as a new mri contrast: findings in rat hippocampus. *Neuroimage* 60, 1380–1393.
- Palombo, M., Ligneul, C., Najac, C., Le Douce, J., Flament, J., Escartin, C., Hantraye, P., Brouillet, E., Bonvento, G., Valette, J., 2016. New paradigm to assess brain cell morphology by diffusion-weighted mr spectroscopy in vivo. *Proceedings of the National Academy of Sciences*, 201504327.
- Paquette, M., Merlet, S., Gilbert, G., Deriche, R., Descoteaux, M., 2015. Comparison of sampling strategies and sparsifying transforms to improve compressed sensing diffusion spectrum imaging. *Magnetic resonance in medicine* 73, 401–416.
- Pizzolato, M., Fick, R., Boutelier, T., Deriche, R., 2016. Noise floor removal via phase correction of complex diffusion-weighted images: Influence on dti and q-space metrics, in: *Computational Diffusion MRI*.
- Price, W.S., 1997. Pulsed-field gradient nuclear magnetic resonance as a tool for studying translational diffusion: Part 1. basic theory. *Concepts in magnetic resonance* 9, 299–336.
- Pyatigorskaya, N., Bihan, D., Reynaud, O., Ciobanu, L., 2014. Relationship between the diffusion time and the diffusion mri signal observed at 17.2 tesla in the healthy rat brain cortex. *Magnetic resonance in medicine* 72, 492–500.
- Quirk, J.D., Bretthorst, G.L., Duong, T.Q., Snyder, A.Z., Springer, C.S., Ackerman, J.J., Neil, J.J., 2003. Equilibrium water exchange between the intra-and extracellular spaces of mammalian brain. *Magnetic resonance in medicine* 50, 493–499.
- Rathi, Y., Michailovich, O., Laun, F., Setsompop, K., Grant, P., Westin, C.F., 2014. Multi-shell diffusion signal recovery from sparse measurements. *Medical image analysis* 18, 1143–1156.
- Ronen, I., Budde, M., Ercan, E., Annese, J., Techawiboonwong, A., Webb, A., 2014. Microstructural organization of axons in the human corpus callosum quantified by diffusion-weighted magnetic resonance spectroscopy of n-acetylaspartate and post-mortem histology. *Brain Structure and Function* 219, 1773–1785.

- St-Jean, S., Coupé, P., Descoteaux, M., 2016. Non local spatial and angular matching: Enabling higher spatial resolution diffusion mri datasets through adaptive denoising. *Medical image analysis* 32, 115–130.
- Stejskal, E., 1965. Use of spin echoes in a pulsed magnetic-field gradient to study anisotropic, restricted diffusion and flow. *The Journal of Chemical Physics* 43, 3597–3603.
- Sun, J., Sakhæe, E., Entezari, A., Vemuri, B.C., 2015. Leveraging eap-sparsity for compressed sensing of ms-hardi in (k, q) -space, in: *Information processing in medical imaging: proceedings of the... conference*, NIH Public Access. p. 375.
- Tanner, J., 1978. Transient diffusion in a system partitioned by permeable barriers. application to nmr measurements with a pulsed field gradient. *The Journal of Chemical Physics* 69, 1748–1754.
- Tanner, J., Stejskal, E.O., 1968. Restricted self-diffusion of protons in colloidal systems by the pulsed-gradient, spin-echo method. *The Journal of Chemical Physics* 49, 1768–1777.
- Tournier, J.D., Calamante, F., Connelly, A., 2007. Robust determination of the fibre orientation distribution in diffusion mri: non-negativity constrained super-resolved spherical deconvolution. *NeuroImage* 35, 1459–1472.
- Tristán-Vega, A., Westin, C.F., Aja-Fernández, S., 2009. Estimation of fiber orientation probability density functions in high angular resolution diffusion imaging. *NeuroImage* 47, 638–650.
- Tuch, D.S., 2004. Q-ball imaging. *Magnetic Resonance in Medicine* 52, 1358–1372.
- Veraart, J., Fieremans, E., Novikov, D.S., 2016. Universal power-law scaling of water diffusion in human brain defines what we see with mri. *arXiv preprint arXiv:1609.09145* .
- Wedeen, V.J., Hagmann, P., Tseng, W.Y.I., Reese, T.G., Weisskoff, R.M., 2005. Mapping complex tissue architecture with diffusion spectrum magnetic resonance imaging. *Magnetic Resonance in Medicine* 54, 1377–1386.
- Wu, Y.C., Field, A.S., Alexander, A.L., 2008. Computation of diffusion function measures in-space using magnetic resonance hybrid diffusion imaging. *Medical Imaging, IEEE Transactions on* 27, 858–865.
- Zou, H., Hastie, T., 2005. Regularization and variable selection via the elastic net. *Journal of the Royal Statistical Society: Series B (Statistical Methodology)* 67, 301–320.
- Zucchelli, M., Brusini, L., Méndez, C.A., Daducci, A., Granziera, C., Menegaz, G., 2016. What lies beneath? diffusion eap-based study of brain tissue microstructure. *Medical image analysis* 32, 145–156.